Eur. Phys. J. C 49, 815–829 (2007)
DOI 10.1140/epjc/s10052-006-0168-4

THE EUROPEAN PHYSICAL JOURNAL C

Regular Article – Theoretical Physics

Tachyonic cascade spectra of supernova remnants and TeV blazars

R. Tomaschitz[a]

Department of Physics, Hiroshima University, 1-3-1 Kagami-yama, Higashi-Hiroshima 739-8526, Japan

Received: 10 August 2006 /
Published online: 10 January 2007 –

Abstract. The superluminal spectral densities of relativistic electrons in uniform motion are derived, semiclassically and in second quantization. The effect of electron spin on the tachyonic radiation field, a Proca field with negative mass-square, is studied. There is a longitudinally polarized spectral component due to the negative mass-square of the tachyonic quanta. The radiation densities are averaged with electron distributions, and high- and low-temperature expansions are obtained. Spectral fits to the γ-ray spectra of the Crab Nebula, the supernova remnant RX J1713.7–3946, and the BL Lacertae objects H1426+428, 1ES 1959+650, Mkn 501, and Mkn 421 are performed. In contrast to TeV photons, the extragalactic tachyon flux is not attenuated by interaction with the background light; there is no absorption of tachyonic γ-rays, as tachyons do not interact with infrared photons. The curvature of the TeV spectra in double-logarithmic plots is caused by the Boltzmann factor of the electron densities generating the tachyon flux. The extended spectral plateau in the GeV band, visible in the spectral maps of the two Galactic supernova remnants as well as in the flare spectra of the BL Lacertae objects, is reproduced by the tachyonic radiation densities. Estimates of the electron populations in the supernova remnants and active galactic nuclei are inferred from the spectral fits, such as power-law indices, electron temperatures, and source counts. Upper bounds on the Lorentz factors in the source populations are derived and compared to the breaks in the high-energy cosmic-ray spectrum.

PACS. 95.30.Gv; 11.10.Lm; 98.70.Sa; 03.50.Kk

1 Introduction

The goal is to find evidence for tachyonic (superluminal) γ-rays in the high-energy spectra of supernova remnants and BL Lacertae (BL Lac) objects. Superluminal radiation is considered in the framework of the Proca equation with negative mass-square [1]. At first sight, the formalism closely resembles electrodynamics, but there are differences as well. Apart from the superluminal speed of the quanta, the radiation is partially longitudinally polarized. A basic feature of photons traveling over cosmological distances is their ability to propagate dispersion free, as the wave fields are conformally coupled to the background metric. This property is also retained for tachyons, as the tachyon mass scales inversely with the cosmic expansion factor. There is no interaction of tachyons with photons; they couple only indirectly via matter fields. Therefore, contrary to electromagnetic γ-rays, high-energy tachyons cannot interact with the infrared background radiation, so that there is no attenuation of the extragalactic tachyon flux due to electron–positron pair creation.

The most pronounced difference between photons and tachyons lies in the emission process itself. Freely moving electrons can radiate superluminal quanta. We already demonstrated this with classical point charges and scalar quantum currents [2]. Here, we include spin, deriving the quantized superluminal spectral densities generated by a Dirac current of freely propagating electrons. Radiation densities attached to a uniformly moving charge have no analog in electrodynamics; their very existence has substantial implications for the space–time structure, requiring an absorber medium [3, 4]. The Green function of this radiation process is time symmetric; there is no retarded propagator supported outside the light cone. The advanced modes of the radiation field are converted into retarded ones by virtue of a nonlocal, instantaneous interaction with the cosmic absorber medium. The latter defines an absolute space–time, a universal frame of reference, necessary to render the superluminal signal transfer causal. The time symmetry of the Green function implies that there is no radiation damping; the radiating charge stays in uniform motion. The energy radiated is supplied by the oscillators constituting the absorber medium [5]. The tachyonic radiation densities depend on the velocity of the uniformly moving charge in the rest frame of the cosmic absorber,

[a] e-mail: tom@geminga.org

and there is a radiation threshold, a minimal speed for superluminal radiation to occur [2]. The absorber medium is absorptive for advanced modes only; there is no attenuation of retarded modes.

The mentioned properties of tachyonic wave propagation have been elaborated in previous papers. Here, we focus on specific applications, apart from Sect. 2, where the spectral densities generated by a Dirac current are derived. It is crucial to have a good conceptual understanding of the spectral densities generated by uniformly moving charges, as there is no analog in electrodynamics, and a good technical command is also needed since other superluminal radiation processes reduce in some limit to this radiation, e.g. tachyonic synchrotron radiation in the limit of infinite bending radius [6]. Electromagnetic synchrotron densities vanish in the zero-magnetic-field limit, of course.

In Sect. 2, we derive the transversal and longitudinal spectral densities of uniformly moving charges. We at first give a semiclassical derivation, based on the correspondence principle, and then recover the semiclassical result in second quantization. We compare to previously derived limit cases, to the superluminal radiation of a classical point charge in uniform motion, as well as to the spectral densities generated by a freely propagating scalar matter field [2]. We then integrate the densities to obtain the power radiated and the tachyonic number count.

In Sect. 3, we average the tachyonic spectral densities with electron distributions. We consider thermal Boltzmann and Fermi distributions, as well as power-law densities with exponential cutoff. In Sect. 4, we derive the high- and low-temperature expansions of the averaged radiation densities and discuss spectral peaks, breaks, slopes, and spectral curvature. In Sect. 5, we perform spectral fits to the γ-ray broadband of two Galactic supernova remnants (SNRs), the Crab Nebula and RX J1713.7–3946, as well as to the flare spectra of the blazars H1426+428, 1ES 1959+650, Mkn 501, and Mkn 421. In this way, we infer the cutoff temperature of the electronic/protonic source populations, compare it to the break energies in the cosmic-ray spectrum, and point out the possibility of ultra-high-energy protons in the supernova remnants. In Sect. 6, we present our conclusions.

2 Tachyonic spectral densities of freely moving electrons

Superluminal radiation emitted by a spin-less charge in arbitrary motion was studied in [2]. The transversal and longitudinal power coefficients were derived,

$$P^{\mathrm{T}}_{mn} = \frac{1}{8\pi^2}\omega_{mn}k_{\mathrm{t}}(\omega_{mn})\int_{|\mathbf{x}|=1}\left|\tilde{\mathbf{J}}^{\mathrm{T}}_{mn}(\mathbf{x})\right|^2\mathrm{d}\Omega\,,$$
$$P^{\mathrm{L}}_{mn} = \frac{m_{\mathrm{t}}^2}{8\pi^2}\frac{k_{\mathrm{t}}(\omega_{mn})}{\omega_{mn}}\int_{|\mathbf{x}|=1}\left|\tilde{\mathbf{J}}^{\mathrm{L}}_{mn}(\mathbf{x})\right|^2\mathrm{d}\Omega\,, \qquad (2.1)$$

accounting for the radiation of a particle descending from an initial state m to a final state n. In this section, we evaluate the coefficients (2.1) for a Dirac current and derive the tachyonic spectral densities of a spinning charge in uniform motion, the power transversally and longitudinally radiated, as well as the tachyonic number counts.

We briefly explain the quantities occurring in the power coefficients (2.1). The tachyonic wave numbers are related to the electron frequencies by $k_{\mathrm{t}}(\omega_{mn}) = \sqrt{\omega_{mn}^2+m_{\mathrm{t}}^2}$, where $\omega_{mn} = \omega_m - \omega_n > 0$ is the energy of the radiated superluminal quanta. The integration is over the solid angle $\mathrm{d}\Omega$. The integrands in (2.1) are defined by the integral transform,

$$\tilde{\mathbf{J}}^{\mathrm{T,L}}_{mn}(\mathbf{x}) := \int \mathrm{d}\mathbf{x}'\tilde{\mathbf{j}}^{\mathrm{T,L}}_{mn}(\mathbf{x}',\mathbf{x})\exp(-\mathrm{i}k_{\mathrm{t}}(\omega_{mn})\mathbf{n}\cdot\mathbf{x}')\,, \quad (2.2)$$

where $\mathbf{n} = \mathbf{x}/r$. The matrices $\tilde{\mathbf{j}}^{\mathrm{T,L}}_{mn}$ denote the transversal/longitudinal current components,

$$\tilde{\mathbf{j}}^{\mathrm{T}}_{mn}(\mathbf{x}',\mathbf{x}) := \tilde{\mathbf{j}}_{mn}(\mathbf{x}') - \tilde{\mathbf{j}}^{\mathrm{L}}_{mn}(\mathbf{x}',\mathbf{x})\,,$$
$$\tilde{\mathbf{j}}^{\mathrm{L}}_{mn}(\mathbf{x}',\mathbf{x}) := \mathbf{n}(\mathbf{n}\cdot\tilde{\mathbf{j}}_{mn}(\mathbf{x}'))\,. \qquad (2.3)$$

The matrix elements of a free, time-separated Dirac current $(\tilde{\rho}_{mn},\tilde{\mathbf{j}}_{mn})$ read, cf. equation (2.13) of [7],

$$\tilde{\rho}_{mn}(\mathbf{x}) = \frac{q}{L^3}\frac{(\omega_m+m)(\omega_n+m)+k_mk_ns_ms_n}{2\sqrt{\omega_m\omega_n(\omega_m+m)(\omega_n+m)}}$$
$$\times\,\varphi'^{\dagger}_n\varphi'_m\,\mathrm{e}^{\mathrm{i}\mathbf{k}_{mn}\mathbf{x}}\,,$$
$$\tilde{\mathbf{j}}_{mn}(\mathbf{x}) = \frac{q}{L^3}\frac{(\omega_m+m)k_ns_n+(\omega_n+m)k_ms_m}{2\sqrt{\omega_m\omega_n(\omega_m+m)(\omega_n+m)}}$$
$$\times\,\varphi'^{\dagger}_n\boldsymbol{\sigma}\varphi'_m\,\mathrm{e}^{\mathrm{i}\mathbf{k}_{mn}\mathbf{x}}\,. \qquad (2.4)$$

The multi-index $n = (\mathbf{k}_n, s_n)$ indicates electron momentum and spin. We consider positive frequencies, and choose periodic boundary conditions on a box of size L, so that $\mathbf{k} = 2\pi\mathbf{n}/L$, with integer lattice points $\mathbf{n}\in Z^3$. In (2.4), we use the shortcuts $\omega_{mn} := \omega_m - \omega_n$, $\mathbf{k}_{mn} := \mathbf{k}_m - \mathbf{k}_n$, and the electronic dispersion relation $k_m = \sqrt{\omega_m^2 - m^2}$. The 2-spinors φ'_m (explicitly given in equation (A.9) of [7]) solve $(\boldsymbol{\sigma}\mathbf{k} - ks)\varphi'_{k,s} = 0$, where $k = |\mathbf{k}|$ is the electronic wave number and s takes the values ±1 for the determinant to vanish. The helicity functions are normalized as $\varphi'^{\dagger}_{k,s}\varphi'_{k,s} = 1$, so that $\int_{L^3}\tilde{\rho}_{mn}\mathrm{d}^3x = q\delta_{mn}$. We also note that $\omega_{mn}\tilde{\rho}_{mn}(0) = \mathbf{k}_{mn}\tilde{\mathbf{j}}_{mn}(0)$ (no summation here). The squared matrix elements read, cf. equation (2.14) of [7],

$$|\tilde{\rho}_{mn}|^2 = \frac{q^2}{L^6}\frac{\omega_m\omega_n+m^2+k_mk_ns_ms_n}{4\omega_m\omega_nk_mk_n}$$
$$\times\,(k_mk_n + s_ms_n\mathbf{k}_m\mathbf{k}_n)\,,$$
$$\left|\tilde{\mathbf{j}}_{mn}\right|^2 = \frac{q^2}{L^6}\frac{\omega_m\omega_n-m^2+k_mk_ns_ms_n}{4\omega_m\omega_nk_mk_n}$$
$$\times\,(3k_mk_n - s_ms_n\mathbf{k}_m\mathbf{k}_n)\,, \qquad (2.5)$$

where we made use of $2\left|\varphi'^{\dagger}_{k,s}\varphi'_{q,r}\right|^2 = 1 + rs\mathbf{k}_0\mathbf{q}_0$ and $2\left|\varphi'^{\dagger}_{k,s}\boldsymbol{\sigma}\varphi'_{q,r}\right|^2 = 3 - rs\mathbf{k}_0\mathbf{q}_0$, cf. equation (A.13) of [7].

They simplify if summed over the 'final' spin s_n, cf. equation (2.15) of [7],

$$\sum_{s_n=\pm1}|\tilde\rho_{mn}|^2=\frac{q^2}{L^6}\frac{\omega_m\omega_n+m^2+\mathbf{k}_m\mathbf{k}_n}{2\omega_m\omega_n}\,,$$
$$\sum_{s_n=\pm1}\left|\tilde{\mathbf{j}}_{mn}\right|^2=\frac{q^2}{L^6}\frac{3\omega_m\omega_n-3m^2-\mathbf{k}_m\mathbf{k}_n}{2\omega_m\omega_n}\,. \quad (2.6)$$

The integral transform of the unpolarized current, $\tilde{\mathbf{J}}_{mn}(\mathbf{x})$, is defined by (2.2), with $\tilde{\mathbf{j}}^{\mathrm{T,L}}_{mn}$ replaced by $\tilde{\mathbf{j}}_{mn}(\mathbf{x}')$. The squared transversal current transform is readily calculated by making use of $\left|\tilde{\mathbf{J}}^{\mathrm{T}}_{mn}\right|^2=\left|\tilde{\mathbf{J}}_{mn}\right|^2-\left|\tilde{\mathbf{J}}^{\mathrm{L}}_{mn}\right|^2$. All norms are vectorial, referring to individual matrix elements, and complex conjugation is implied when squaring vectors. The matrices $\tilde{\mathbf{J}}^{\mathrm{T,L}}_{mn}(\mathbf{x})$ depend only on the unit vector $\mathbf{n}=\mathbf{x}/r$. The longitudinal component, $\tilde{\mathbf{J}}^{\mathrm{L}}_{mn}(\mathbf{x})$, is determined by the charge density,

$$\tilde{\mathbf{J}}^{\mathrm{L}}_{mn}(\mathbf{x})=\mathbf{n}\,\omega_{mn}k_{\mathrm{t}}^{-1}(\omega_{mn})\int\mathrm{d}\mathbf{x}'\tilde\rho_{mn}(\mathbf{x}')$$
$$\times\exp(-\mathrm{i}k_{\mathrm{t}}(\omega_{mn})\mathbf{n}\cdot\mathbf{x}')\,. \quad (2.7)$$

This can easily be checked by substituting the continuity equation, $\mathrm{i}\omega_{mn}\tilde\rho_{mn}(\mathbf{x})=\nabla\tilde{\mathbf{j}}_{mn}(\mathbf{x})$, and applying the Gauss theorem.

If we consider free currents such as (2.4), the integrations in (2.2) and (2.7) can readily be carried out,

$$\tilde{\mathbf{J}}_{mn}(\mathbf{x})=(2\pi)^3\tilde{\mathbf{j}}_{mn}(0)\,\delta(\mathbf{K}_{mn},L)\,,$$
$$(2\pi)^3\delta(\mathbf{k},L):=\int_{L^3}\mathrm{e}^{\mathrm{i}\mathbf{k}\mathbf{x}}\mathrm{d}\mathbf{x}\,,$$
$$\tilde{\mathbf{J}}^{\mathrm{L}}_{mn}(\mathbf{x})=(2\pi)^3\mathbf{n}\omega_{mn}k_{\mathrm{t}}^{-1}(\omega_{mn})\tilde\rho_{mn}(0)\delta(\mathbf{K}_{mn},L)\,,$$
$$\mathbf{K}_{mn}:=\mathbf{k}_{mn}-k_{\mathrm{t}}(\omega_{mn})\mathbf{n}\,,\quad \mathbf{k}_{mn}:=\mathbf{k}_m-\mathbf{k}_n\,. \quad (2.8)$$

Here, the electronic wave vector is denoted by $\mathbf{k}_m$ or $\mathbf{k}_n$, the subscripts indicating initial and final states, and $\mathbf{k}$ stands for the tachyonic wave vector, occasionally with a subscript 't' attached. The electronic and tachyonic dispersion relations read $k_m=\sqrt{\omega_m^2-m^2}$ and $k_{\mathrm{t}}(\omega_{mn})=\sqrt{\omega_{mn}^2+m_{\mathrm{t}}^2}$, respectively. The electronic wave vectors are discretized in a box of size L, cf. after (2.4). The truncated δ-function $\delta(\mathbf{k},L)$ is a standard limit definition of the Dirac function, $\delta(\mathbf{k},L\to\infty)=\delta(\mathbf{k})$. When squaring the current transforms (2.8) in the integrands of the power coefficients (2.1), we substitute $(2\pi/L)^3\delta^2(\mathbf{k},L)=\delta(\mathbf{k},L)$. This identity holds for $L\to\infty$, that is, both sides are limit definitions of $\delta(\mathbf{k})$. The solid angle integration $\mathrm{d}\Omega$ in (2.1) refers to the unit vector $\mathbf{n}=\mathbf{x}/r$, which enters into the integrands only through $\delta(\mathbf{K}_{mn},L)$. In the limit $L\to\infty$,

$$\int_{|\mathbf{x}|=1}\delta(\mathbf{K}_{mn},L)\mathrm{d}\Omega=2k_{\mathrm{t}}^{-1}(\omega_{mn})\delta\big(\mathbf{k}_{mn}^2-k_{\mathrm{t}}^2(\omega_{mn})\big)\,, \quad (2.9)$$

where the integration is done by means of the substitution $\int_{|\mathbf{x}|=1}\mathrm{d}\Omega\to2\int_{R^3}\mathrm{d}^3\mathbf{n}\delta(\mathbf{n}^2-1)$. In this way, we find explicit formulas for the power coefficients (2.1) generated by a free current,

$$P^{\mathrm{T}}_{mn}=\frac{(2\pi L)^3}{4\pi^2}\frac{\omega_{mn}}{k_{\mathrm{t}}^2(\omega_{mn})}\Big(k_{\mathrm{t}}^2(\omega_{mn})\big|\tilde{\mathbf{j}}_{mn}\big|^2-\omega_{mn}^2\big|\tilde\rho_{mn}\big|^2\Big)$$
$$\times\,\delta\big(\mathbf{k}_{mn}^2-k_{\mathrm{t}}^2(\omega_{mn})\big)\,,$$
$$P^{\mathrm{L}}_{mn}=\frac{(2\pi L)^3}{4\pi^2}\frac{m_{\mathrm{t}}^2\omega_{mn}}{k_{\mathrm{t}}^2(\omega_{mn})}\,|\tilde\rho_{mn}|^2\,\delta\big(\mathbf{k}_{mn}^2-k_{\mathrm{t}}^2(\omega_{mn})\big)\,. \quad (2.10)$$

Here, we substitute the squared matrix elements (2.5). The multi-indices m and n are defined after (2.4).

The total power radiated is found by summing the coefficients (2.10) over the final states and performing the continuum limit,

$$P^{\mathrm{T,L}}=\sum\nolimits_{\mathbf{k}_n,s_n}P^{\mathrm{T,L}}_{mn},$$
$$\mathrm{d}P^{\mathrm{T,L}}=L^3(2\pi)^{-3}\sum\nolimits_{s_n}P^{\mathrm{T,L}}_{mn}\mathrm{d}^3\mathbf{k}_n\,. \quad (2.11)$$

We introduce polar coordinates for $\mathbf{k}_n$, with $\mathbf{k}_m$ as polar axis, replace $\mathrm{d}^3\mathbf{k}_n$ by $2\pi k_n^2\mathrm{d}k_n\int_{-1}^1\mathrm{d}\cos\theta$, and integrate $\mathrm{d}P^{\mathrm{T,L}}$ over the polar angle, arriving at

$$\mathrm{d}P^{\mathrm{T}}(k_n)=\frac{L^6}{4\pi k_m}\frac{\omega_{mn}}{k_{\mathrm{t}}^2(\omega_{mn})}\sum_{s_n=\pm1}\Big(k_{\mathrm{t}}^2(\omega_{mn})\big|\tilde{\mathbf{j}}_{mn}\big|^2$$
$$-\omega_{mn}^2\,|\tilde\rho_{mn}|^2\Big)\,\Theta(D_{mn})k_n\mathrm{d}k_n\,,$$
$$\mathrm{d}P^{\mathrm{L}}(k_n)=\frac{L^6}{4\pi k_m}\frac{m_{\mathrm{t}}^2\omega_{mn}}{k_{\mathrm{t}}^2(\omega_{mn})}\sum_{s_n=\pm1}|\tilde\rho_{mn}|^2\Theta(D_{mn})k_n\mathrm{d}k_n\,. \quad (2.12)$$

The argument in the Heaviside function is

$$D_{mn}:=4k_m^2k_n^2-\left(k_m^2+k_n^2-k_{\mathrm{t}}^2(\omega_{mn})\right)^2\,. \quad (2.13)$$

The squared matrix elements in (2.12) are those stated in (2.5) and (2.6), supplemented by the insertion

$$\mathbf{k}_m\mathbf{k}_n\to\frac{1}{2}\big(k_m^2+k_n^2-k_{\mathrm{t}}^2(\omega_{mn})\big)$$
$$\equiv\omega_m^2-\omega_0^2-\frac{1}{4}m_{\mathrm{t}}^2-\omega_m\omega_{mn}\,, \quad (2.14)$$

where ω_0 is defined in (2.16). Both the step function $\Theta(D_{mn})$ and this substitution in the matrix elements are a consequence of the δ-function in (2.10). The latter greatly facilitates the $\mathrm{d}\cos\theta$ integration by virtue of $\mathbf{k}_m\mathbf{k}_n=k_mk_n\cos\theta$ in its argument. The identity in (2.14) follows from the dispersion relations stated after (2.8).

The initial electronic state is indicated by a subscript m, the final state by n, so that we only need to consider positive ω_{mn}, cf. after (2.1). Making use of the dispersion relations, we write D_{mn} in (2.13) as

$$\frac{1}{4m_{\mathrm{t}}^2}D_{mn}=\omega_m^2-\omega_0^2-\omega_m\omega_{mn}-\frac{m^2}{m_{\mathrm{t}}^2}\omega_{mn}^2\,. \quad (2.15)$$

D_{mn} is positive only if $\omega_{mn}<\omega_{\max}$, where

$$\omega_{\max}:=\sqrt{\omega_m^2-m^2}\frac{\omega_0}{m}\frac{m_{\mathrm{t}}}{m}-\frac{1}{2}\omega_m\frac{m_{\mathrm{t}}^2}{m^2}\,,$$
$$\omega_0:=m\sqrt{1+\frac{1}{4}\frac{m_{\mathrm{t}}^2}{m^2}}\,. \tag{2.16}$$

This $\omega_{\max}$ is a zero of $D_{mn}(\omega_{mn})$, and a positive $\omega_{\max}$ requires $\omega_m>\omega_0$. Thus, in the case of uniform motion, the energy ω_m of the radiating charge has to surpass the threshold ω_0 for superluminal radiation to occur. The spectral range is $0<\omega_{mn}<\omega_{\max}$, determined by $\Theta(D_{mn})=1$ in the power differentials (2.12).

We integrate the differentials (2.12) to find the power, $P^{\mathrm{T,L}}=\int_0^{k_m}\mathrm{d}P^{\mathrm{T,L}}(k_n)$, and to identify the spectral densities. To this end, we introduce ω_{mn} as integration variable, $\omega_n\mathrm{d}\omega_{mn}=-k_n\mathrm{d}k_n$, by virtue of the electronic dispersion relation. We write ω for ω_{mn}, and define $p^{\mathrm{T,L}}(\omega)\mathrm{d}\omega:=-\mathrm{d}P^{\mathrm{T,L}}(\omega_{mn})$, so that $P^{\mathrm{T,L}}=\int_0^{\omega_{\max}}p^{\mathrm{T,L}}(\omega)\mathrm{d}\omega$. The transversal and longitudinal spectral densities $p^{\mathrm{T,L}}(\omega)$ can be read off from (2.12) and the squared matrix elements (2.6) (with (2.14) substituted),

$$p^{\mathrm{T}}(\omega)=\frac{q^2}{4\pi}\frac{m_{\mathrm{t}}^2}{\omega_m k_m}\frac{\omega}{\omega^2+m_{\mathrm{t}}^2}\times\left(\omega_m^2-m^2+\frac{1}{4}m_{\mathrm{t}}^2-\omega_m\omega-\left(\frac{m^2}{m_{\mathrm{t}}^2}-\frac{1}{2}\right)\omega^2\right)\,, \tag{2.17}$$

$$p^{\mathrm{L}}(\omega)=\frac{q^2}{4\pi}\frac{m_{\mathrm{t}}^2}{\omega_m k_m}\frac{\omega}{\omega^2+m_{\mathrm{t}}^2}\left(\omega_m^2-\frac{1}{4}m_{\mathrm{t}}^2-\omega_m\omega\right)\,. \tag{2.18}$$

To summarize, ω_m and $k_m=\sqrt{\omega_m^2-m^2}$ denote the energy and wave number of the radiating electron, and $\omega_m>\omega_0$. The electronic threshold energy ω_0 depends on the electron–tachyon mass ratio, cf. (2.16). The frequencies radiated range over $0<\omega<\omega_{\max}$. The tachyonic spectral densities $p^{\mathrm{T,L}}(\omega)$ are cut off at the break frequency $\omega_{\max}$ defined in (2.16). The units $\hbar=c=1$ can easily be restored. We use the Heaviside–Lorentz system, so that $\alpha_{\mathrm{e}}=e^2/(4\pi\hbar c)\approx 1/137$ and $\alpha_{\mathrm{q}}=q^2/(4\pi\hbar c)\approx 1.0\times10^{-13}$ are the electric and tachyonic fine structure constants. We also note the ratio $\alpha_{\mathrm{q}}/\alpha_{\mathrm{e}}\approx 1.4\times10^{-11}$ and the tachyon mass $m_{\mathrm{t}}\approx m/238\approx 2.15\,\mathrm{keV}/c^2$. These estimates are obtained from hydrogenic Lamb shifts [1]. Finally, if we substitute the matrix elements (squared and subjected to (2.14)) of a free Klein–Gordon current,

$$\tilde\rho_{mn}(\mathbf{x})=\frac{q}{L^3}\frac{\omega_m+\omega_n}{2\sqrt{\omega_m\omega_n}}\mathrm{e}^{\mathrm{i}\mathbf{k}_{mn}\mathbf{x}}\,,$$
$$\tilde{\mathbf{j}}_{mn}(\mathbf{x})=\frac{q}{L^3}\frac{\mathbf{k}_m+\mathbf{k}_n}{2\sqrt{\omega_m\omega_n}}\mathrm{e}^{\mathrm{i}\mathbf{k}_{mn}\mathbf{x}}\,, \tag{2.19}$$

into the power coefficients (2.12) and drop the spin summations there, we arrive at very similarly structured densities, cf. [2] and after (2.24). $\omega_{\max}$ and in particular the threshold ω_0 remain unchanged.

Remark: the spectral densities (2.17) and (2.18) are derived from the classical power coefficients (2.1) by invoking the correspondence principle. This amounts to identifying $\tilde\rho_{mn}(0)$ and $\tilde{\mathbf{j}}_{mn}(0)$ in (2.8) and (2.10) with the Hermitian current matrices $\tilde\rho_{mn}$ and $\tilde{\mathbf{j}}_{mn}$ in (2.4) and (2.5), and to performing the spin summation in (2.12) according to (2.6). It is easy to check that the densities (2.17) and (2.18) also hold in second quantization. The power coefficients (2.1) can be recovered from the spontaneous transversal and longitudinal emission rates $\mathrm{d}w_{\mathrm{em}}^{\mathrm{T,sp}}$ and $\mathrm{d}w_{\mathrm{em},T=0}^{\mathrm{L,sp}}$ calculated in equations (3.12) and (3.16) of [7]. We substitute the free charge and current matrices $\tilde\rho_{mn}$ and $\tilde{\mathbf{j}}_{mn}$, cf. (2.4), for the matrices $\rho_{mr,ns}$ and $\mathbf{j}_{mr,ns}$ occurring in equations (3.10)–(3.16) of [7]. We consider unpolarized transversal radiation, which means replacing $\boldsymbol{\varepsilon}_{\mathbf{k},\lambda}\mathbf{j}_{mr,ns}$ in $\mathrm{d}w_{\mathrm{em}}^{\mathrm{T,sp}}$ by the transversal current $\mathbf{j}_{mr,ns}^{\mathrm{T}}=\mathbf{j}_{mr,ns}-\mathbf{k}_0(\mathbf{k}_0\mathbf{j}_{mr,ns})$, where $\mathbf{k}_0$ is the tachyonic unit wave vector, cf. equations (3.11) and (3.12) of [7]. The angularly integrated transversal and longitudinal emission at $\omega=\omega_{mn}$ is $P_{mn}^{\mathrm{T}}=\hbar\omega_{mn}\int_\Omega\mathrm{d}w_{\mathrm{em}}^{\mathrm{T,sp}}$ and $P_{mn}^{\mathrm{L}}=\hbar\omega_{mn}\int_\Omega\mathrm{d}w_{\mathrm{em},\,T=0}^{\mathrm{L,sp}}$, which coincides with the power coefficients (2.1) after restoring the units there.

An elementary integration of the energy densities (2.17) and (2.18) gives the transversally and longitudinally radiated power as defined before (2.17),

$$P^{\mathrm{T,L}}=\frac{1}{2}\frac{q^2}{4\pi}\frac{m^2m_{\mathrm{t}}^2}{\omega_m\sqrt{\omega_m^2-m^2}}\left[\left(\frac{\omega_m^2}{m^2}-\frac{1}{4}\frac{m_{\mathrm{t}}^2}{m^2}\right)\times\log\left(1+\frac{\omega_{\max}^2}{m_{\mathrm{t}}^2}\right)-\frac{\omega_{\max}^2}{m_{\mathrm{t}}^2}\left(M^{\mathrm{T,L}}-\frac{1}{4}\frac{m_{\mathrm{t}}^2}{m^2}\right)+2\frac{\omega_m}{m}\frac{m_{\mathrm{t}}}{m}\left(\arctan\frac{\omega_{\max}}{m_{\mathrm{t}}}-\frac{\omega_{\max}}{m_{\mathrm{t}}}\right)\right]\,,$$
$$M^{\mathrm{T}}:=1-\frac{1}{4}\frac{m_{\mathrm{t}}^2}{m^2}\,,\quad M^{\mathrm{L}}:=\frac{1}{4}\frac{m_{\mathrm{t}}^2}{m^2}\,. \tag{2.20}$$

Here, ω_m stands for the electron energy $m\gamma$ and $0<\arctan<\pi/2$. The total power radiated is obtained by adding the polarization components, $P^{\mathrm{T}}+P^{\mathrm{L}}$. Similarly, the tachyonic number counts $N^{\mathrm{T,L}}$ (tachyons radiated per unit time) are found by integrating the number densities, $n^{\mathrm{T,L}}(\omega):=p^{\mathrm{T,L}}(\omega)/(\hbar\omega)$, up to $\omega_{\max}$,

$$N^{\mathrm{T,L}}=\frac{q^2}{4\pi}\frac{m^2m_{\mathrm{t}}}{\omega_m\sqrt{\omega_m^2-m^2}}\left[\left(\frac{\omega_m^2}{m^2}-\frac{1}{4}\frac{m_{\mathrm{t}}^2}{m^2}\right)\arctan\frac{\omega_{\max}}{m_{\mathrm{t}}}-\frac{\omega_{\max}}{m_{\mathrm{t}}}\left(M^{\mathrm{T,L}}-\frac{1}{4}\frac{m_{\mathrm{t}}^2}{m^2}\right)-\frac{1}{2}\frac{\omega_m}{m}\frac{m_{\mathrm{t}}}{m}\times\log\left(1+\frac{\omega_{\max}^2}{m_{\mathrm{t}}^2}\right)\right]\,. \tag{2.21}$$

To obtain the energy flux and the number flux, we have to normalize by dividing $P^{\mathrm{T,L}}$ and $N^{\mathrm{T,L}}$ by $4\pi d^2$, where d is the distance to the source; the differential fluxes are found by normalizing the respective densities, cf. Sect. 5.

To figure out the terms generated by the electron spin, we compare to a free scalar charge with current matrix (2.19), cf. [2]. In the power components (2.20) and count rates (2.21), we only have to replace the $M^{\mathrm{T,L}}$ terms (defined in (2.20)) by $M_{\mathrm{sc}}^{\mathrm{T}}=1+m_{\mathrm{t}}^2/(4m^2)$ and $M_{\mathrm{sc}}^{\mathrm{L}}=0$, respectively, to recover the radiation from a scalar particle in uniform motion. The phenomenological discussion

in [2] carries over to spinning particles, including the three asymptotic regimes elaborated there, the ultra-relativistic, nonrelativistic, and extreme nonrelativistic limit at the radiation threshold ω_0.

In Sect. 3, we average the radiation densities (2.17) and (2.18) with electron distributions. To this end, we parameterize them with the electronic Lorentz factor, writing $\omega_m = m\gamma$, so that

$$p^{\mathrm{T,L}}(\omega,\gamma) = \frac{q^2}{4\pi}\frac{m_{\mathrm{t}}^2\omega}{\omega^2+m_{\mathrm{t}}^2}\left[\gamma^2 - \frac{m_{\mathrm{t}}}{m}\frac{\omega}{m_{\mathrm{t}}}\gamma + \frac{1}{4}\frac{m_{\mathrm{t}}^2}{m^2}\frac{\omega^2}{m_{\mathrm{t}}^2} - \left(1+\frac{\omega^2}{m_{\mathrm{t}}^2}\right)M^{\mathrm{T,L}}\right]\frac{1}{\gamma\sqrt{\gamma^2-1}}, \tag{2.22}$$

where $M^{\mathrm{T}} = 1 - M^{\mathrm{L}}$ and $M^{\mathrm{L}} = m_{\mathrm{t}}^2/(4m^2)$ as in (2.20). The spectral cutoff occurs at

$$\omega_{\max}(\gamma) = m_{\mathrm{t}}\left(\mu\sqrt{\gamma^2-1} - \frac{1}{2}\frac{m_{\mathrm{t}}}{m}\gamma\right), \quad \mu := \sqrt{1+m_{\mathrm{t}}^2/(4m^2)}\,. \tag{2.23}$$

At the cutoff frequency,

$$p^{\mathrm{T}}(\omega_{\max}) = \frac{1}{2}\frac{m_{\mathrm{t}}^2}{m^2}p^{\mathrm{L}}(\omega_{\max}), \quad p^{\mathrm{L}}(\omega_{\max}) = \frac{q^2}{4\pi}\frac{\omega_{\max}}{\gamma\sqrt{\gamma^2-1}}. \tag{2.24}$$

We recover from (2.22) the spectral densities generated by a Klein–Gordon current (2.19), if we replace $M^{\mathrm{T,L}}$ by $M_{\mathrm{sc}}^{\mathrm{T,L}}$ as defined after (2.21); $\omega_{\max}$ remains unchanged. The spectral densities of a classical point charge [2] are recovered by putting all m_{t}/m ratios in (2.22) and (2.23) equal to zero,

$$p_{\mathrm{cl}}^{\mathrm{T,L}}(\omega,\gamma) = \frac{q^2}{4\pi}\frac{m_{\mathrm{t}}^2\omega}{\omega^2+m_{\mathrm{t}}^2}\left[\gamma^2 - \left(1+\frac{\omega^2}{m_{\mathrm{t}}^2}\right)M_{\mathrm{cl}}^{\mathrm{T,L}}\right]\times\frac{1}{\gamma\sqrt{\gamma^2-1}}. \tag{2.25}$$

Here, $M_{\mathrm{cl}}^{\mathrm{T}} = 1$ and $M_{\mathrm{cl}}^{\mathrm{L}} = 0$, and the classical spectral cutoff occurs at $\omega_{\max,\mathrm{cl}} := m_{\mathrm{t}}\sqrt{\gamma^2-1}$. In the ultra-relativistic limit, $\gamma \gg 1$, we can likewise drop all terms containing m_{t}/m ratios in (2.22) and (2.23), so that the ultra-relativistic quantum densities coalesce with the classical densities (2.25).

The radiation condition $\omega_m > \omega_0$ on the electron energy, cf. after (2.16), translates into $\gamma > \mu$ for the Lorentz factor, with μ in (2.23). The threshold on the speed of the charge for radiation to occur is thus $\upsilon > \upsilon_{\min} := m_{\mathrm{t}}/(2m\mu)$. The tachyon–electron mass ratio, $m_{\mathrm{t}}/m \approx 1/238$, cf. after (2.18), gives $\upsilon_{\min}/c \approx 2.1\times 10^{-3}$.

3 Spectral averaging with Boltzmann and Fermi power laws

The radiation densities (2.22) are generated by single charges. We average them with electron distributions such as power-law densities, $\mathrm{d}\rho \propto E^{-2-\alpha}\mathrm{d}^3p$, parameterized with the Lorentz factor, $\mathrm{d}\rho \propto \gamma^{-1-\alpha}\sqrt{\gamma^2-1}\mathrm{d}\gamma$, by means of $E = m\gamma$ and $p = m\sqrt{\gamma^2-1}$. A thermal Boltzmann distribution, $\mathrm{d}\rho \propto \mathrm{e}^{-E/(kT)}\mathrm{d}^3p$, admits the parameterization $\mathrm{d}\rho \propto \mathrm{e}^{-\beta\gamma}\sqrt{\gamma^2-1}\gamma\mathrm{d}\gamma$, with $\beta := mc^2/(kT)$. A Fermi distribution is obtained by replacing $\mathrm{e}^{-\beta\gamma} \to 1/(\mathrm{e}^{\beta\gamma}+1)$. We consider hybrid averages, power laws exponentially cut with Boltzmann and Fermi distributions,

$$\mathrm{d}\rho_{\alpha,\beta}^{\mathrm{B}}(\gamma) := \gamma^{-\alpha-1}\mathrm{e}^{-\beta\gamma}\sqrt{\gamma^2-1}\mathrm{d}\gamma, \tag{3.1}$$

$$\mathrm{d}\rho_{\alpha,\beta}^{\mathrm{F}}(\gamma) := \gamma^{-\alpha-1}\frac{\sqrt{\gamma^2-1}}{\mathrm{e}^{\beta\gamma}+1}\mathrm{d}\gamma. \tag{3.2}$$

The electronic Lorentz factors range in an interval $\gamma_1 \le \gamma < \infty$, where the lower edge satisfies the radiation condition $\gamma_1 \ge \mu$, $\mu := \sqrt{1+m_{\mathrm{t}}^2/(4m^2)}$, cf. after (2.25). Only particles with Lorentz factors exceeding the threshold μ can radiate superluminal quanta, cf. after (2.16). The normalization factors $A_{\alpha,\beta}^{\mathrm{B,F}}(\gamma_1,n_1)$ of these densities are determined by $n_1 = A_{\alpha,\beta}^{\mathrm{B,F}}(\gamma_1,n_1)\int_{\gamma_1}^{\infty}\mathrm{d}\rho_{\alpha,\beta}^{\mathrm{B,F}}(\gamma)$, where n_1 is the electron count and γ_1 the smallest Lorentz factor of the source population. For notational convenience, we have not included the normalization factors in the distributions (3.1) and (3.2). We will also consider averages over multiple electron populations, for instance,

$$\mathrm{d}\rho = \lambda_1\mathrm{d}\rho_{-2,\beta_1}^{\mathrm{F}} + \lambda_2\mathrm{d}\rho_{\alpha_2,\beta_2}^{\mathrm{B}}, \tag{3.3}$$

a thermal fermionic density and a power-law Boltzmann density. Such linear combinations, including pure power laws, cf. (4.12), have been used to model γ-ray burst spectra [8–10] and electron distributions in galaxy clusters [11].

The averaging is carried out via

$$\langle p^{\mathrm{T,L}}(\omega;\gamma_1,n_1)\rangle_{\alpha,\beta}^{\mathrm{B,F}} := A_{\alpha,\beta}^{\mathrm{B,F}}(\gamma_1,n_1)\int_{\gamma_1}^{\infty}p^{\mathrm{T,L}}(\omega,\gamma)\times\theta(\omega_{\max}(\gamma)-\omega)\mathrm{d}\rho_{\alpha,\beta}^{\mathrm{B,F}}(\gamma), \tag{3.4}$$

with $\omega_{\max}(\gamma)$ in (2.23). These averages can be reduced to the spectral functions [12]

$$B^{\mathrm{T,L}}(\omega;\gamma;\alpha,\beta) := \int_{\gamma}^{\infty}p^{\mathrm{T,L}}(\omega,\tilde\gamma)\mathrm{d}\rho_{\alpha,\beta}^{\mathrm{B}}(\tilde\gamma), \tag{3.5}$$

$$F^{\mathrm{T,L}}(\omega;\gamma;\alpha,\beta) := \int_{\gamma}^{\infty}p^{\mathrm{T,L}}(\omega,\tilde\gamma)\mathrm{d}\rho_{\alpha,\beta}^{\mathrm{F}}(\tilde\gamma), \tag{3.6}$$

where $\gamma \ge \mu$. More explicitly,

$$B^{\mathrm{T,L}}(\omega;\gamma;\alpha,\beta) = \frac{q^2}{4\pi}\frac{m_{\mathrm{t}}\hat\omega}{1+\hat\omega^2}\frac{1}{\gamma^{\alpha+1}\beta^2}\times\left\{\left[(1+\alpha)\alpha+\beta\gamma(1+\alpha)\frac{m_{\mathrm{t}}}{m}\frac{\hat\omega}{\gamma}-(\beta\gamma)^2\frac{Q^{\mathrm{T,L}}(\hat\omega)}{\gamma^2}\right](\beta\gamma)^{\alpha+1}\right.$$
$$\left.\times\Gamma(-\alpha-1,\beta\gamma) - \left[\alpha-\beta\gamma\left(1-\frac{m_{\mathrm{t}}}{m}\frac{\hat\omega}{\gamma}\right)\right]\mathrm{e}^{-\beta\gamma}\right\}, \tag{3.7}$$

where $\hat\omega := \omega/m_\mathrm{t}$ and

$$Q^{\mathrm{T,L}}(\hat\omega) := (1+\hat\omega^2)M^{\mathrm{T,L}} - \frac{1}{4}\frac{m_\mathrm{t}^2}{m^2}\hat\omega^2 \equiv (1+\hat\omega^2)\Delta^{\mathrm{T,L}} + \frac{1}{4}\frac{m_\mathrm{t}^2}{m^2}, \tag{3.8}$$

$$M^\mathrm{T} = 1-\frac{1}{4}\frac{m_\mathrm{t}^2}{m^2}, \quad M^\mathrm{L} = \frac{1}{4}\frac{m_\mathrm{t}^2}{m^2}, \quad \Delta^{\mathrm{T,L}} := M^{\mathrm{T,L}} - \frac{1}{4}\frac{m_\mathrm{t}^2}{m^2}. \tag{3.9}$$

We note that $\Delta^\mathrm{T} = 1-m_\mathrm{t}^2/(2m^2)$ and $\Delta^\mathrm{L}=0$. The integration in (3.6) gives

$$F^{\mathrm{T,L}}(\omega;\gamma;\alpha,\beta) = \frac{q^2}{4\pi}\frac{m_\mathrm{t}\hat\omega}{1+\hat\omega^2}\beta^{\alpha-1}\left[\Gamma_\mathrm{F}(-\alpha+1,\beta\gamma) - \frac{m_\mathrm{t}}{m}\frac{\hat\omega}{\gamma}\beta\gamma\Gamma_\mathrm{F}(-\alpha,\beta\gamma) - \frac{Q^{\mathrm{T,L}}(\hat\omega)}{\gamma^2}(\beta\gamma)^2\Gamma_\mathrm{F}(-\alpha-1,\beta\gamma)\right], \tag{3.10}$$

where we use $Q^{\mathrm{T,L}}(\hat\omega)$ in (3.8) as well as the fermionic counterpart to the incomplete Γ function,

$$\beta^\alpha\Gamma_\mathrm{F}(-\alpha,\beta\gamma) := \int_\gamma^\infty \frac{\gamma^{-\alpha-1}\mathrm{d}\gamma}{1+\mathrm{e}^{\beta\gamma}} = \sum_{n=1}^\infty (-)^{n+1}(n\beta)^\alpha\Gamma(-\alpha,n\beta\gamma). \tag{3.11}$$

The Boltzmann average $B^{\mathrm{T,L}}$ in (3.7) is recovered from $F^{\mathrm{T,L}}$ in (3.10) by replacing Γ_F by Γ.

The spectral range of the radiation densities (2.22) is $0<\omega<\omega_\mathrm{max}(\gamma)$, cf. (2.23). Inversely, the condition $\omega_\mathrm{max}(\hat\gamma)-\omega=0$ or

$$\hat\gamma(\omega) = \mu\sqrt{1+\hat\omega^2} + \frac{1}{2}\frac{m_\mathrm{t}}{m}\hat\omega, \quad \hat\omega := \frac{\omega}{m_\mathrm{t}}, \quad \mu := \sqrt{1+\frac{m_\mathrm{t}^2}{4m^2}} \tag{3.12}$$

defines the minimal electronic Lorentz factor for radiation at this frequency. That is, an electron in uniform motion can radiate at ω only if its Lorentz factor exceeds $\hat\gamma(\omega)$. We also note the identity

$$\hat\gamma^2 - \frac{m_\mathrm{t}}{m}\hat\omega\hat\gamma = 1+\hat\omega^2+\frac{m_\mathrm{t}^2}{4m^2}. \tag{3.13}$$

With these prerequisites, the averages (3.4) can readily be assembled. The lower edge of Lorentz factors in the electron distribution defines the break frequency $\omega_1 := \omega_\mathrm{max}(\gamma_1)$, separating the spectrum into a low- and a high-frequency band. More explicitly, cf. (2.23),

$$\hat\omega_1 = \mu\sqrt{\gamma_1^2-1} - \frac{1}{2}\frac{m_\mathrm{t}}{m}\gamma_1, \tag{3.14}$$

where $\hat\omega_1 = \omega_1/m_\mathrm{t}$. Hence, $\hat\gamma(\omega_1)=\gamma_1$, and $\hat\gamma(\omega)>\gamma_1$ if $\omega>\omega_1$, cf. (3.12). ($\gamma_1=\mu$ corresponds to $\omega_1=0$.)

In the low-frequency band, $\omega\le\omega_1$, the Boltzmann-averaged energy density (3.4) reads

$$\left\langle p^{\mathrm{T,L}}(\omega;\gamma_1,n_1)\right\rangle^\mathrm{B}_{\alpha,\beta} = A^\mathrm{B}_{\alpha,\beta}(\gamma_1,n_1)B^{\mathrm{T,L}}(\omega;\gamma_1;\alpha,\beta), \tag{3.15}$$

with the spectral function $B^{\mathrm{T,L}}$ in (3.7). In the upper frequency band, $\omega\ge\omega_1$, we find that

$$\left\langle p^{\mathrm{T,L}}(\omega;\gamma_1,n_1)\right\rangle^\mathrm{B}_{\alpha,\beta} = A^\mathrm{B}_{\alpha,\beta}(\gamma_1,n_1)B^{\mathrm{T,L}}(\omega;\hat\gamma(\omega);\alpha,\beta), \tag{3.16}$$

with $\hat\gamma(\omega)$ in (3.12). We may combine this to give

$$\left\langle p^{\mathrm{T,L}}(\omega;\gamma_1,n_1)\right\rangle^\mathrm{B}_{\alpha,\beta} = A^\mathrm{B}_{\alpha,\beta}(\gamma_1,n_1) \times\left[B^{\mathrm{T,L}}(\omega;\gamma_1;\alpha,\beta)\theta(\omega_1-\omega) + B^{\mathrm{T,L}}(\omega;\hat\gamma(\omega);\alpha,\beta)\theta(\omega-\omega_1)\right], \tag{3.17}$$

which is the explicit evaluation of the Boltzmann average (3.4), valid for all frequencies $0\le\omega\le\infty$. The same relations (3.15)–(3.17) hold true for the Fermi average $\langle p^{\mathrm{T,L}}(\omega;\gamma_1,n_1)\rangle^\mathrm{F}_{\alpha,\beta}$ in (3.4), if we replace the spectral function $B^{\mathrm{T,L}}$ by the fermionic counterpart $F^{\mathrm{T,L}}$ in (3.10), and the normalization factor $A^\mathrm{B}_{\alpha,\beta}$ by $A^\mathrm{F}_{\alpha,\beta}$, cf. after (3.2).

The tachyonic number density (tachyons emitted per unit time and unit frequency interval) is related to the energy density (3.17) by

$$\left\langle n^{\mathrm{T,L}}(\omega;\gamma_1,n_1)\right\rangle^\mathrm{B}_{\alpha,\beta} := \frac{1}{\omega}\langle p^{\mathrm{T,L}}(\omega;\gamma_1,n_1)\rangle^\mathrm{B}_{\alpha,\beta}. \tag{3.18}$$

The superscripts T and L denote the transversal and longitudinal polarization components, cf. Sect. 2, so that $\langle n^\mathrm{T}\rangle^\mathrm{B}_{\alpha,\beta}$ is the transversal count rate and $\langle p^\mathrm{T}\rangle^\mathrm{B}_{\alpha,\beta}$ the energy transversally radiated. If the polarization is not distinguished, we add the polarization components, writing $\langle n^{\mathrm{T+L}}\rangle^\mathrm{B}_{\alpha,\beta}$ for the unpolarized count; the phenomenological discussion of γ-ray spectra in Sect. 5 is centered on the ω^2-rescaled unpolarized count.

4 High- and low-temperature asymptotics of the averaged radiation densities

4.1 Boltzmann averages

To obtain the low-temperature expansion, $\beta\to\infty$, of the Boltzmann average (3.17), we substitute the asymptotic expansion of the incomplete Γ function into the spectral function $B^{\mathrm{T,L}}(\omega;\gamma;\alpha,\beta)$ in (3.7),

$$(\beta\gamma)^{\alpha+1}\Gamma(-\alpha-1,\beta\gamma) \sim \frac{\mathrm{e}^{-\beta\gamma}}{\beta\gamma}\left[1-\frac{2+\alpha}{\beta\gamma}+\frac{(2+\alpha)(3+\alpha)}{(\beta\gamma)^2}-\cdots\right]. \tag{4.1}$$

This series terminates for integer $\alpha \le -2$ and is then exact. Collecting powers, we find that

$$B^{\mathrm{T,L}}(\omega;\gamma;\alpha,\beta) \sim \frac{q^2}{4\pi}\frac{m_{\mathrm{t}}\hat{\omega}}{1+\hat{\omega}^2}\frac{\mathrm{e}^{-\beta\gamma}}{\gamma^\alpha\beta} \times\left[C_0^{\mathrm{T,L}}(\gamma)+\frac{C_1^{\mathrm{T,L}}(\gamma)}{\beta\gamma}+\frac{C_2^{\mathrm{T,L}}(\gamma)}{(\beta\gamma)^2}+\cdots\right], \tag{4.2}$$

with coefficients

$$\begin{aligned} C_0^{\mathrm{T,L}}(\gamma) &:= 1-\frac{m_{\mathrm{t}}}{m}\frac{\hat{\omega}}{\gamma}-\frac{Q^{\mathrm{T,L}}(\hat{\omega})}{\gamma^2}\,,\\ C_1^{\mathrm{T,L}}(\gamma) &:= -\alpha+(1+\alpha)\frac{m_{\mathrm{t}}}{m}\frac{\hat{\omega}}{\gamma}+(2+\alpha)\frac{Q^{\mathrm{T,L}}(\hat{\omega})}{\gamma^2}\,,\\ C_2^{\mathrm{T,L}}(\gamma) &:= \alpha(1+\alpha)-(1+\alpha)(2+\alpha)\frac{m_{\mathrm{t}}}{m}\frac{\hat{\omega}}{\gamma}\\ &\quad -(2+\alpha)(3+\alpha)\frac{Q^{\mathrm{T,L}}(\hat{\omega})}{\gamma^2}\,. \end{aligned} \tag{4.3}$$

This holds for Lorentz factors $\gamma \ge \mu$, cf. after (3.2). The expansion parameter is $\beta\gamma \gg 1$. Substituting $\hat{\gamma}(\omega)$ for γ, cf. (3.12) and (3.13), we find that $C_0^{\mathrm{T,L}}(\hat{\gamma}(\omega)) = (1-\Delta^{\mathrm{T,L}})(1+\hat{\omega}^2)/\hat{\gamma}^2$, so that $C_0^{\mathrm{T}}(\hat{\gamma}) = \mathrm{O}(m_{\mathrm{t}}^2/m^2)$; the leading order in the $1/(\beta\gamma)$ expansion of the transversal distribution (3.16) can be smaller than the next-to-leading order. If $\beta \gg 1$ and $\gamma_1 = \mu$, the spectral peak of $\langle p^{\mathrm{T,L}}(\omega;\gamma_1,n_1)\rangle^{\mathrm{B}}_{\alpha,\beta}$, cf. (3.17), occurs at very small $\hat{\omega}$, owing to the exponential in (4.2), so that we can expand in $\hat{\omega}$. The maximum is therefore determined by the factor $\hat{\omega}\,\mathrm{e}^{-\beta\hat{\gamma}}$ and is located at

$$\hat{\omega}_{\max} \approx \sqrt{\xi^2+\frac{1}{\beta\mu}}-\xi\,,\quad \xi := \frac{1}{4\mu}\frac{m_{\mathrm{t}}}{m}\,, \tag{4.4}$$

so that $\hat{\omega}_{\max} \approx 1/\sqrt{\beta\mu}$, if $\beta\xi^2 \ll 1$. In the opposite limit, $\beta\xi^2 \gg 1$, we find that $\hat{\omega}_{\max} \approx 1/(2\beta\xi\mu)$. The peak at $\hat{\omega}_{\max}$ is followed by exponential decay; there is no power-law tail. If $\beta \gg 1$ and $\gamma_1 \gg 1$, the peak of the densities (3.17) is determined by the factor $\hat{\omega}/(1+\hat{\omega}^2)$ in (4.2) and occurs at $\hat{\omega}_{\max} \approx 1$. It is followed by power-law decay, $B^{\mathrm{T,L}} \propto 1/\hat{\omega}$, in the range $1 \ll \hat{\omega} \ll \gamma_1$. At about $\hat{\omega} \approx \gamma_1$, exponential decay sets in.

We turn to the high-temperature expansion of $B^{\mathrm{T,L}}$ in (3.7), based on

$$(\beta\gamma)^{\alpha+1}\Gamma(-\alpha-1,\beta\gamma) = (\beta\gamma)^{\alpha+1}\Gamma(-\alpha-1)+\frac{1}{\alpha+1}-\frac{\beta\gamma}{\alpha} +\frac{(\beta\gamma)^2}{2!(\alpha-1)}-\cdots. \tag{4.5}$$

High-temperature expansions always require $\beta\gamma \ll 1$. In the opposite limit, $\beta\gamma \gg 1$, we may still use the low-temperature expansion (4.2), even if $\beta \ll 1$. We also note that the series

$$(\beta\gamma)^{\alpha+1}\Gamma(-\alpha-1,\beta\gamma) \sim (\beta\gamma)^{\alpha+1}\Gamma(-\alpha-1) +\frac{\mathrm{e}^{-\beta\gamma}}{\alpha+1}\left(1-\frac{\beta\gamma}{\alpha}+\frac{(\beta\gamma)^2}{\alpha(\alpha-1)}-\cdots\right) \tag{4.6}$$

is the asymptotic low-temperature expansion replacing (4.1) if both $\beta\gamma$ and $|\alpha|$ are large and $\beta\gamma/|\alpha| \ll 1$; we will not consider this limit here, assuming moderate electronic power-law indices. The high-temperature expansion of $B^{\mathrm{T,L}}(\omega;\gamma;\alpha,\beta)$ follows from the series (4.5),

$$\begin{aligned} B^{\mathrm{T,L}}(\omega;\gamma;\alpha,\beta) &= \frac{q^2}{4\pi}\frac{m_{\mathrm{t}}\hat{\omega}}{1+\hat{\omega}^2}\gamma^{1-\alpha}\left\{(\beta\gamma)^{\alpha-1}\Gamma(-\alpha-1)\right.\\ &\quad\times\left[(1+\alpha)\alpha+\beta\gamma(1+\alpha)\frac{m_{\mathrm{t}}}{m}\frac{\hat{\omega}}{\gamma}-(\beta\gamma)^2\frac{Q^{\mathrm{T,L}}(\hat{\omega})}{\gamma^2}\right]\\ &\quad\left.+D_0^{\mathrm{T,L}}-\beta\gamma D_1^{\mathrm{T,L}}+\frac{(\beta\gamma)^2}{2!}D_2^{\mathrm{T,L}}-\cdots\right\}. \end{aligned} \tag{4.7}$$

We here use the shortcut

$$D_n^{\mathrm{T,L}}(\hat{\omega};\gamma,\alpha) := \frac{1}{\alpha-n-1}-\frac{m_{\mathrm{t}}}{m}\frac{\hat{\omega}}{\gamma}\frac{1}{\alpha-n} -\frac{Q^{\mathrm{T,L}}(\hat{\omega})}{\gamma^2}\frac{1}{\alpha-n+1}\,. \tag{4.8}$$

Singularities occurring at integer α cancel if ε-expanded [12].

The averages of the classical densities (2.25) are obtained by dropping all terms depending on m_{t}/m ratios in (3.7)–(3.9) as well as (4.2) and (4.7). In particular, $\mu = 1$, $\hat{\gamma}(\omega) = \sqrt{1+\omega^2/m_{\mathrm{t}}^2}$, and $\omega_1 = m_{\mathrm{t}}\sqrt{\gamma_1^2-1}$, cf. (3.12) and (3.14). The first two orders of the low-temperature expansion of the classical $B^{\mathrm{T,L}}$ thus read, cf. (4.2),

$$B^{\mathrm{T,L}}(\omega;\gamma;\alpha,\beta) \sim \frac{q^2}{4\pi}\frac{m_{\mathrm{t}}^2\omega}{\omega^2+m_{\mathrm{t}}^2}\frac{\mathrm{e}^{-\beta\gamma}}{\gamma^\alpha\beta} \times\left[\left(1-\frac{\Delta^{\mathrm{T,L}}}{\gamma^2}\frac{\omega^2+m_{\mathrm{t}}^2}{m_{\mathrm{t}}^2}\right) +\frac{1}{\beta\gamma}\left((2+\alpha)\frac{\Delta^{\mathrm{T,L}}}{\gamma^2}\frac{\omega^2+m_{\mathrm{t}}^2}{m_{\mathrm{t}}^2}-\alpha\right)+\cdots\right], \tag{4.9}$$

with $\Delta^{\mathrm{T}} = 1$ and $\Delta^{\mathrm{L}} = 0$; the leading order vanishes in $B^{\mathrm{T}}(\omega;\hat{\gamma}(\omega);\alpha,\beta)$.

At high temperature, we find in lowest order in $\beta\gamma$, if $\alpha > 1$,

$$B^{\mathrm{T,L}}(\omega;\gamma;\alpha,\beta) \sim \frac{q^2}{4\pi}\frac{m_{\mathrm{t}}^2\omega}{\omega^2+m_{\mathrm{t}}^2}\frac{\gamma^{1-\alpha}}{\alpha-1} \times\left(1-\frac{\alpha-1}{\alpha+1}\frac{\Delta^{\mathrm{T,L}}}{\gamma^2}\frac{\omega^2+m_{\mathrm{t}}^2}{m_{\mathrm{t}}^2}\right). \tag{4.10}$$

This is valid up to terms of $\mathrm{O}(\beta\gamma,(\beta\gamma)^{\alpha-1})$. (If $\alpha > 1$, the $D_0^{\mathrm{T,L}}$ term in (4.7) gives the dominant contribution stated in (4.10); the term containing the m_{t}/m ratio in $D_0^{\mathrm{T,L}}$ has been dropped.)

If $\gamma_1 = \mu$, the maximum of $\langle p^{\mathrm{T,L}}(\omega;\gamma_1,n_1)\rangle^{\mathrm{B}}_{\alpha,\beta}$ is determined by the leading factor $\propto \omega\hat{\gamma}^{-\alpha-1}$ in (4.10), and is located at $\omega_{\max} \approx m_{\mathrm{t}}/\sqrt{\alpha}$. (This $\omega_{\max}$ is not to be confused with the spectral cutoff $\omega_{\max}(\gamma)$ in (2.23).) The peak is followed by power-law decay $\propto \omega^{-\alpha}$ for $\omega \ll m_{\mathrm{t}}/\beta$ and exponential decay starting at about $\omega \approx m_{\mathrm{t}}/\beta$. The low-temperature expansion (4.9) applies for $\omega \gg m_{\mathrm{t}}/\beta$.

If $\gamma_1 \gg 1$ (but still $\beta\gamma_1 \ll 1$), the peak of $\langle p^{\mathrm{T,L}}(\omega;\gamma_1, n_1)\rangle^{\mathrm{B}}_{\alpha,\beta}$ in (3.17) is determined by the factor $\omega/(\omega^2+m_{\mathrm{t}}^2)$ in (4.10) and occurs at $\omega_{\max}\approx m_{\mathrm{t}}$. It is followed by power-law decay, $\langle p^{\mathrm{T,L}}\rangle^{\mathrm{B}}_{\alpha,\beta}\propto 1/\omega$, in the range $1\ll\omega/m_{\mathrm{t}}\ll\gamma_1$, which turns into $\langle p^{\mathrm{T,L}}\rangle^{\mathrm{B}}_{\alpha,\beta}\propto\omega^{-\alpha}$ in the interval $\gamma_1<\omega/m_{\mathrm{t}}\ll 1/\beta$. At $\omega\approx m_{\mathrm{t}}/\beta$, there is an exponential cutoff according to (4.9). In Sect. 5, we consider the E^2-rescaled flux density $E^2\mathrm{d}N^{\mathrm{T,L}}/\mathrm{d}E$, which is related to the energy density $\langle p^{\mathrm{T,L}}\rangle^{\mathrm{B}}_{\alpha,\beta}$ as stated in (5.1). The preceding scaling relations for $\langle p^{\mathrm{T,L}}\rangle^{\mathrm{B}}_{\alpha,\beta}$ give a plateau value $E^2\mathrm{d}N^{\mathrm{T,L}}/\mathrm{d}E\propto 1$ in the range $1\ll E/(m_{\mathrm{t}}c^2)\ll\gamma_1$, followed by power-law decay $E^2\mathrm{d}N^{\mathrm{T,L}}/\mathrm{d}E\propto E^{1-\alpha}$ in the band $\gamma_1<E/(m_{\mathrm{t}}c^2)\ll 1/\beta$, and subsequent exponential decay.

The foregoing discussion is based on (4.10), and thus requires an electron index $\alpha>1$. We now turn to $\alpha<1$, which means replacing (4.10) by

$$B^{\mathrm{T,L}}(\omega;\gamma;\alpha,\beta)\sim\frac{q^2}{4\pi}\frac{m_{\mathrm{t}}^2\omega}{\omega^2+m_{\mathrm{t}}^2}\beta^{\alpha-1}\Gamma(1-\alpha)\,. \tag{4.11}$$

This approximation of (4.7) is valid up to terms of $\mathrm{O}(\beta\gamma,(\beta\gamma)^{1-\alpha})$. The spectral peak at $\omega_{\max}\approx m_{\mathrm{t}}$ is again determined by the factor $\omega/(\omega^2+m_{\mathrm{t}}^2)$. Adjacent is a power-law slope $\langle p^{\mathrm{T,L}}\rangle^{\mathrm{B}}_{\alpha,\beta}\propto 1/\omega$ in the range $1\ll\omega/m_{\mathrm{t}}\ll 1/\beta$, so that $E^2\mathrm{d}N^{\mathrm{T,L}}/\mathrm{d}E\propto 1$, cf. (5.1). At $\omega\approx m_{\mathrm{t}}/\beta$, there is the crossover to exponential decay, cf. (4.9). This holds true for $\gamma_1=\mu$ as well as $\gamma_1\gg 1$, provided that $\beta\gamma_1\ll 1$, since the leading order (4.11) does not depend on γ. If the latter condition is not met, that is, if $\beta\gamma_1\gg 1$ despite β being small, then the low-temperature expansion (4.9) applies instead of (4.11). The spectral functions $B^{\mathrm{T,L}}$ in (4.9)–(4.11) are the leading order approximations of the low- and high-temperature expansions (4.2) and (4.7), except that all terms containing the mass ratio m_{t}/m are dropped. The approximations (4.9)–(4.11) are meant as a qualitative overview; they are insufficient in the crossover region $\beta\gamma=\mathrm{O}(1)$. In the spectral maps in Sect. 5, we use the exact spectral functions (3.10).

For electron indices $\alpha>1$, we may consider the limit $\beta=0$ in (3.1), a pure power-law average with density $\mathrm{d}\rho^{\mathrm{B}}_{\alpha,0}\propto E^{-2-\alpha}\mathrm{d}^3p$. The integration (3.5) is elementary if performed with $d\rho^{\mathrm{B}}_{\alpha,0}(\gamma)$ in (3.1),

$$B^{\mathrm{T,L}}(\omega;\gamma;\alpha,0)=\frac{q^2}{4\pi}\frac{m_{\mathrm{t}}\hat{\omega}}{1+\hat{\omega}^2}\gamma^{1-\alpha} \times\left(\frac{1}{\alpha-1}-\frac{m_{\mathrm{t}}}{m}\frac{\hat{\omega}}{\gamma}\frac{1}{\alpha}-\frac{Q^{\mathrm{T,L}}(\hat{\omega})}{\gamma^2}\frac{1}{\alpha+1}\right), \tag{4.12}$$

where $Q^{\mathrm{T,L}}(\hat{\omega})$ is defined in (3.8). This power-law average can also be recovered as the $\beta\to 0$ limit of (4.7). In [13, 14], we studied the ultra-relativistic limit of (4.12), approximating $\mathrm{d}\rho^{\mathrm{B}}_{\alpha,0}\sim\gamma^{-\alpha}\mathrm{d}\gamma$. We used the classical density (2.25) and averaged over finite energy shells $[\gamma_1,\gamma_2]$, $1\ll\gamma_1\ll\gamma_2$, corresponding to $B^{\mathrm{T,L}}(\omega;\gamma_1;\alpha,0)-B^{\mathrm{T,L}}(\omega;\gamma_2;\alpha,0)$ in (3.5). (Here, we may use (4.12) even for $\alpha<1$.) We found that averages over finite energy shells can well reproduce the observed spectral plateaus and power-law slopes. To generate spectral curvature, a smooth exponential cutoff in the electron spectrum is required.

4.2 Fermi averages

The fermionic spectral function $F^{\mathrm{T,L}}$ in (3.10) can be traced back to the Boltzmann average $B^{\mathrm{T,L}}$ in (3.7) via

$$F^{\mathrm{T,L}}(\omega;\gamma;\alpha,\beta)=\sum_{n=1}^{\infty}(-1)^{n+1}B^{\mathrm{T,L}}(\omega;\gamma;\alpha,n\beta)\,. \tag{4.13}$$

This series is efficient for large $\beta\gamma$, since in this case $B^{\mathrm{T,L}}(\omega;\gamma;\alpha,n\beta)\propto\mathrm{e}^{-n\beta\gamma}$, cf. (4.2). The low-temperature expansion of $F^{\mathrm{T,L}}$ is thus given by (4.13) with the low-temperature expansion (4.2) of $B^{\mathrm{T,L}}$ substituted.

The high-temperature expansion of $F^{\mathrm{T,L}}(\omega;\gamma;\alpha,\beta)$ is based on (3.10) and the integral representation of Γ_{F} in (3.11). First,

$$\begin{aligned}\beta^{\alpha}\Gamma_{\mathrm{F}}(-\alpha,\beta\gamma)&=\left(\int_0^{\infty}-\int_0^{\gamma}\right)\frac{\gamma^{-\alpha-1}\mathrm{d}\gamma}{1+\mathrm{e}^{\beta\gamma}} \\ &=\beta^{\alpha}\Gamma_{\mathrm{F}}(-\alpha)+\frac{1}{2}\gamma^{-\alpha}\left(\frac{1}{\alpha}-\frac{1}{2}\frac{\beta\gamma}{\alpha-1}+\frac{1}{24}\frac{(\beta\gamma)^3}{\alpha-3}-\cdots\right),\end{aligned} \tag{4.14}$$

where

$$\Gamma_{\mathrm{F}}(s):=\Gamma(s)\zeta(s)(1-2^{1-s})\,. \tag{4.15}$$

This is the counterpart to expansion (4.5), and the series is to be continued according to the Euler expansion,

$$\begin{aligned}\frac{2}{1+\mathrm{e}^{\beta\gamma}}&=1+2\sum_{n=1}^{\infty}(\beta\gamma)^{2n-1}\frac{1-2^{2n}}{(2n)!}B_{2n} \\ &=1-\frac{1}{2}\beta\gamma+\frac{1}{24}(\beta\gamma)^3-\cdots,\end{aligned} \tag{4.16}$$

where B_{2n} are Bernoulli numbers. By substituting (4.14) into (3.10), we find that

$$\begin{aligned}F^{\mathrm{T,L}}(\omega;\gamma;\alpha,\beta)=\frac{q^2}{4\pi}\frac{m_{\mathrm{t}}\hat{\omega}}{1+\hat{\omega}^2}\gamma^{1-\alpha}\Bigg\{&(\beta\gamma)^{\alpha-1} \\ &\times\left[\Gamma_{\mathrm{F}}(-\alpha+1)-\beta\gamma\frac{m_{\mathrm{t}}}{m}\frac{\hat{\omega}}{\gamma}\Gamma_{\mathrm{F}}(-\alpha)\right. \\ &\left.-(\beta\gamma)^2\frac{Q^{\mathrm{T,L}}(\hat{\omega})}{\gamma^2}\Gamma_{\mathrm{F}}(-\alpha-1)\right] \\ &+\frac{1}{2}\left[D_0^{\mathrm{T,L}}-\frac{\beta\gamma}{2}D_1^{\mathrm{T,L}}+\frac{(\beta\gamma)^3}{24}D_2^{\mathrm{T,L}}-\cdots\right]\Bigg\},\end{aligned} \tag{4.17}$$

with Γ_{F} in (4.15). The series continues as in (4.16), with coefficients $D_n^{\mathrm{T,L}}(\hat{\omega};\gamma,\alpha)$ defined in (4.8). Expansion (4.17) is valid for all α; the singularities occurring for integer $\alpha\geq -1$ in the Γ_{F} functions and the $D_n^{\mathrm{T,L}}$ coefficients cancel each other if ε-expanded. In the case of a thermal Fermi distribution, $\alpha=-2$, we use $\Gamma_{\mathrm{F}}(1)=\log 2$.

If we replace in (4.17) the fermionic $\Gamma_{\rm F}$ by the ordinary Γ function and generate the $D_n^{\rm T,L}$ series with $2\,{\rm e}^{-\beta\gamma}$ instead of (4.16), we recover the Boltzmann average (4.7). The discussions following (4.3), (4.10), and (4.11) regarding spectral peaks, slopes, and exponential cutoffs in the low- and high-temperature limits remain valid for Fermi averages. The spectral maps in Sect. 5 are Boltzmann averages, although Fermi averages can be used as well, with the same parameters. In the resolution of the figures, they are virtually indistinguishable, even in the crossover region.

5 Tachyonic spectral fits to γ-ray spectra of supernova remnants and BL Lac objects

We fit the γ-ray spectra of Galactic supernova remnants and active galactic nuclei (AGNs) with tachyonic cascade spectra assembled from the radiation densities in Sect. 3. We study the γ-ray wideband spectra of the Crab Nebula and SNR RX J1713.7–3946, cf. Figures 1 and 2, as well as flare spectra of the BL Lacs H1426+428, 1ES 1959+650, Mkn 501, and Mkn 421, cf. Figures 3–6. The spectral maps show the ω^2-rescaled tachyonic number flux,

$$E^2\frac{{\rm d}N^{\rm T,L}(E;\alpha,\beta,\gamma_1,n_1)}{{\rm d}E}:=\frac{\omega}{4\pi d^2}\langle p^{\rm T,L}(\omega;\gamma_1,n_1)\rangle^{\rm B}_{\alpha,\beta}\,, \tag{5.1}$$

where $\langle p^{\rm T,L}\rangle^{\rm B}_{\alpha,\beta}$ is the averaged energy density (3.17) and d the distance to the source. The superscript B indicates a Boltzmann average, but the following applies to Fermi averages (3.2) as well. We restore the natural units on the right-hand side of (5.1); up to now we have used $\hbar=c=1$. The proper dimensions are recovered by substituting $\omega_{(1)}\to\hbar\omega_{(1)}=:E_{(1)}$, $m_{(\rm t)}\to m_{(\rm t)}c^2$, $\hat\omega_{(1)}\to E_{(1)}/(m_{\rm t}c^2)$, and $q^2/(4\pi)\to\alpha_{\rm q}/\hbar$ into (3.7), (3.12), (3.14), and (3.17). $\alpha_{\rm q}$ is the tachyonic fine structure constant, cf. after (2.18). The spectral maps in Figs. 2–6 are in TeV units, with the differential tachyon flux ${\rm d}N^{\rm T,L}/{\rm d}E$ in units of ${\rm TeV}^{-1}\,{\rm s}^{-1}\,{\rm cm}^{-2}$. The Crab γ-ray broadband in Fig. 1 is scaled to MeV units. The normalization factor in (3.17) is dimensionless, $A^{\rm B}_{\alpha,\beta}=n_1/\int_{\gamma_1}^\infty {\rm d}\rho^{\rm B}_{\alpha,\beta}(\gamma)$. Here, n_1 is the number of radiating electrons with Lorentz factors exceeding γ_1, distributed according to density ${\rm d}\rho^{\rm B}_{\alpha,\beta}$ in (3.1). α is the electronic power-law index, and β is the exponential cutoff in the electron spectrum, both to be determined from the spectral fit like n_1 and γ_1. As for the electron count n_1, it is convenient to use a rescaled parameter $\hat n_1$ for the fit [15],

$$\hat n_1:=\frac{\alpha_{\rm q}n_1}{\hbar[{\rm keV\ s}]\ 4\pi d^2[{\rm cm}]}\approx 1.27\times10^{-39}\frac{n_1}{d^2[{\rm kpc}]}\,, \tag{5.2}$$

which determines the amplitude of the tachyon flux. Here, $\hbar[{\rm keV\ s}]$ implies the tachyon mass in keV units, that is, $m_{\rm t}c^2\approx 2.15$ in the spectral function (3.7). The purpose of this rescaling is to avoid the uncertain distance estimate in the actual fitting procedure. Once

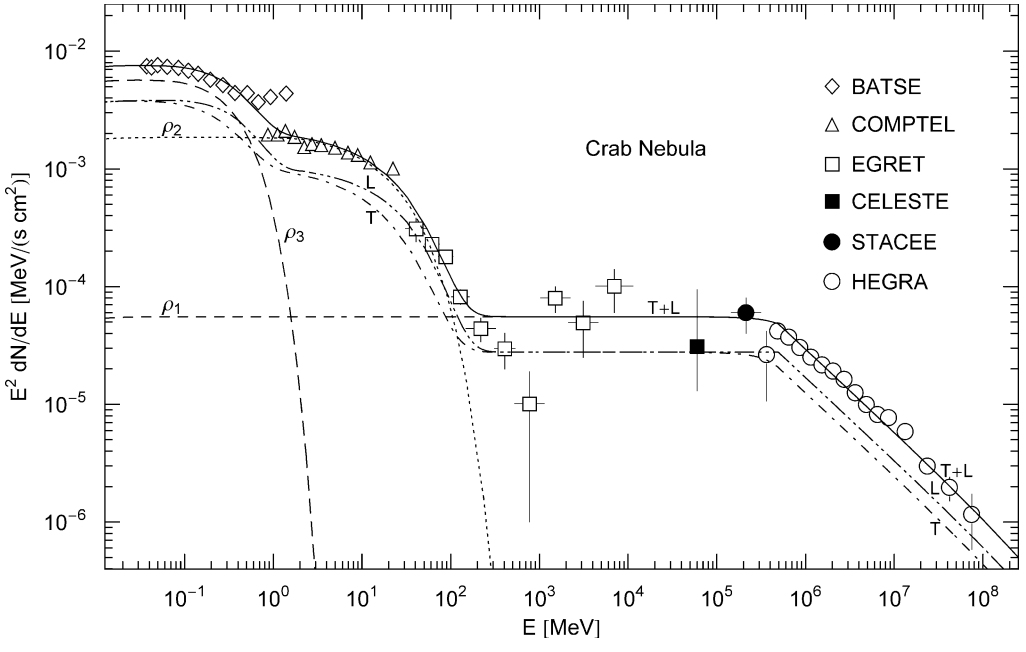

Fig. 1. γ-ray wideband of the Crab Nebula, unpulsed emission. Data points from BATSE [22], COMPTEL [23] (see also [24, 25]), EGRET [23, 26], CELESTE [27], STACEE [28], and HEGRA [29, 30]. The *solid line* T + L stands for the unpolarized differential tachyon flux ${\rm d}N^{\rm T+L}/{\rm d}E$, rescaled with E^2 for better visibility. The transversal and longitudinal flux components, ${\rm d}N^{\rm T,L}/{\rm d}E$, are drawn as *dot-dashed* (T) and *double-dot-dashed* (L) *curves*. The cascade spectra labeled by $\rho_{i=1,2,3}$ (*dotted and dashed lines*) are the unpolarized flux densities ${\rm d}N^{\rm T+L}(E,\rho_i)/{\rm d}E$ of three electron populations ρ_i, cf. Table 1 and after (5.3). All fluxes are rescaled with E^2. The cascades add up to the total flux T + L, which is the actual spectral fit with parameters (of the electron densities ρ_i) recorded in Table 1. The tachyonic spectral map of the pulsed emission is depicted in [15]

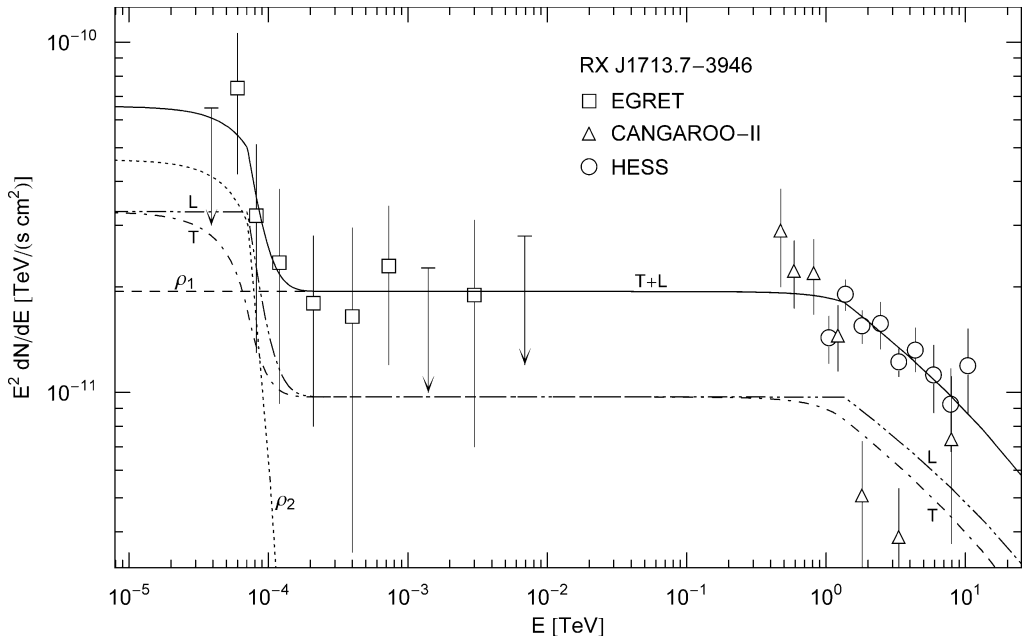

Fig. 2. γ-ray spectrum of SNR RX J1713.7–3946. Data points from EGRET [26, 31], CANGAROO [32], and HESS [33, 34]. The plots are labeled as in Fig. 1. The spectral fit T + L is found by adding the cascade spectra $\rho_{1,2}$ (unpolarized) of two electron populations with parameters listed in Table 1. Adjacent to the GeV plateau is a nearly straight TeV power-law slope. In contrast to the thermal spectra in Figs. 3–6, the cutoff temperature of the ρ_1 cascade in Figs. 1 and 2 is too high to significantly curve the power-law slope in the range covered by the TeV data points. The *solid line* T + L is the unpolarized flux; the transversal and longitudinal flux components are labeled T and L. Two spectral breaks are visible as edges in the longitudinal spectral map, at the break frequencies defined by γ in Table 1, cf. (3.14)

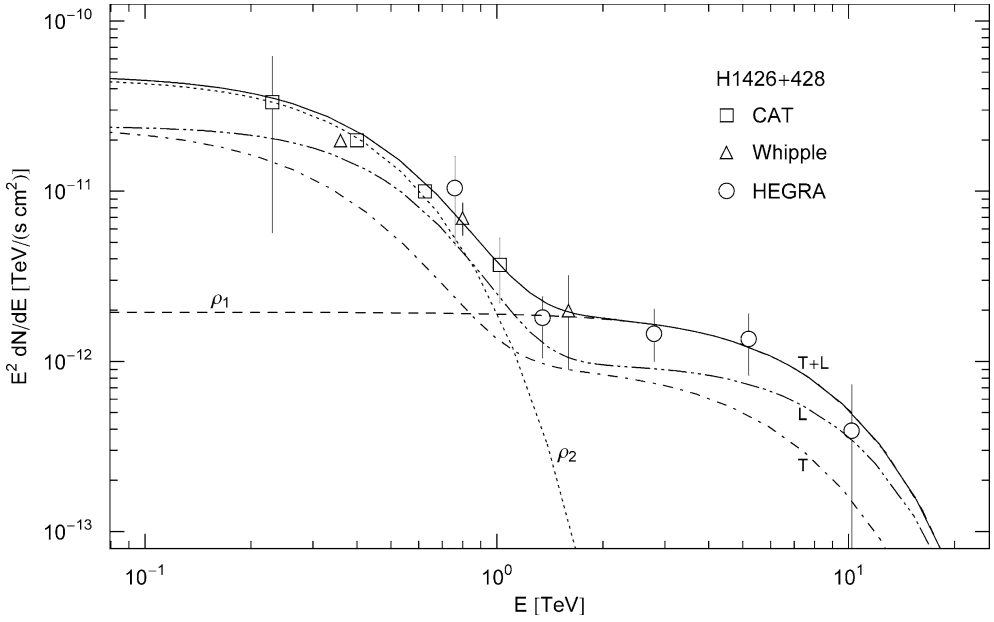

Fig. 3. Spectral map of the BL Lac object H1426+428 (at $z \approx 0.129$). Data points from CAT [35], Whipple [36], and HEGRA [37]. The fit (*solid line* T + L) is obtained by adding the cascades $\rho_{1,2}$ generated by electron densities defined in Table 1. ρ_1 is the cascade producing the TeV spectrum. In this range, ρ_2 is exponentially decaying and does not contribute. The high end of the GeV spectrum is generated by adding the flux of the ρ_2 population to the ρ_1 plateau. The spectral fit T + L is for unpolarized radiation and can be split into a transversally (T) and a longitudinally (L) polarized flux

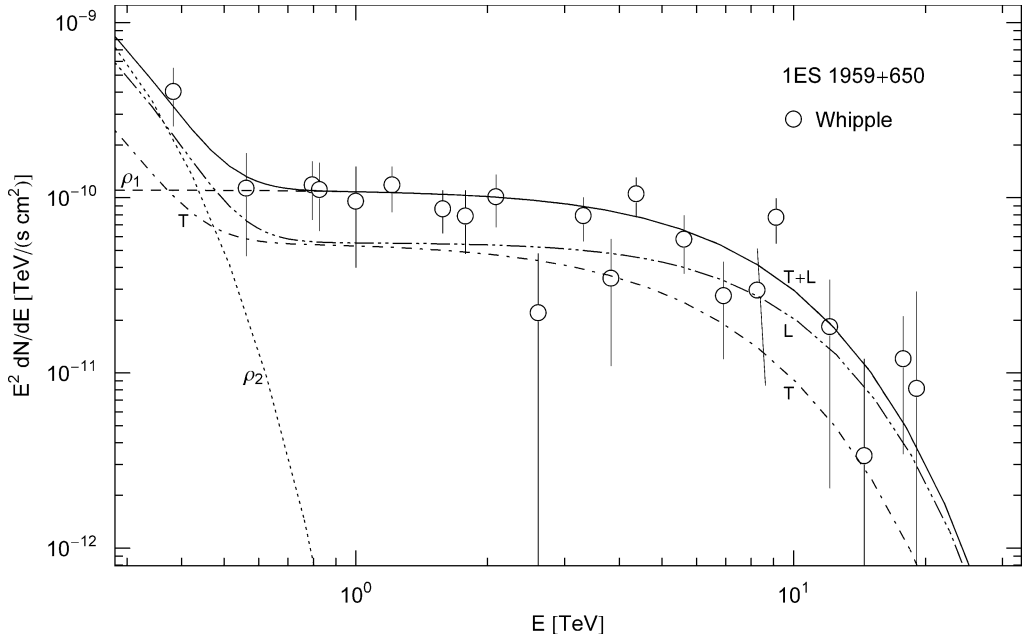

Fig. 4. BL Lac 1ES 1959+650 (at $z \approx 0.047$). Data points from Whipple [38], see also [39]. The spectral fit T + L is composed of two cascades $\rho_{1,2}$. The parameters of the respective electron distributions are recorded in Table 1. The fluxes labeled T and L are the polarization components of the unpolarized fit T + L. The spectral plateau is more extended than in Fig. 3, but there is no substantial change in the TeV band regarding curvature. The electron populations producing the flare spectra in Figs. 3–6 are all thermal; the spectral curvature is generated by the Boltzmann factor in the averaged radiation densities, cf. (4.2)

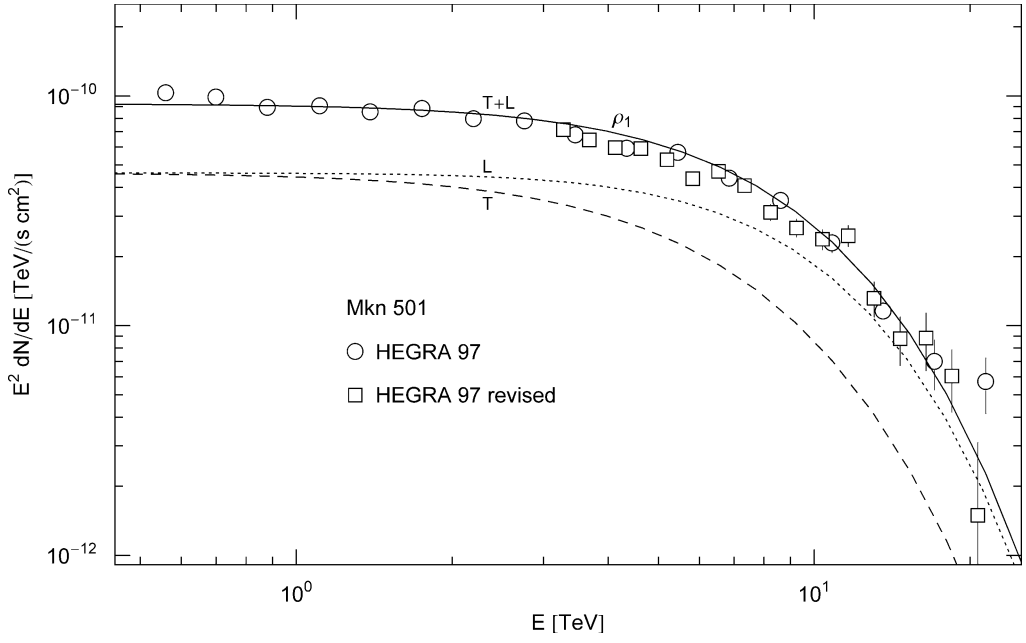

Fig. 5. BL Lac Mkn 501 ($z \approx 0.034$). Data points from HEGRA [40], revised points from [41]. The revised data points are not taken into account in the spectral fit, as the revision is based on intergalactic absorption, assuming electromagnetic γ-rays. The tachyonic γ-ray flux is not attenuated by interaction with infrared background photons. The labeling of the curves is the same as in the previous figures. The spectral fit T + L is a single cascade ρ_1, radiated by an electron population listed in Table 1

$\hat{n}_1$ is known, we can calculate via (5.2) the number of radiating electrons n_1 constituting the density $\mathrm{d}\rho^{\mathrm{B}}_{\alpha,\beta}$. This, however, implies that all tachyons reaching the detector are properly counted. At γ-ray energies, only a tiny $\alpha_{\mathrm{q}}/\alpha_{\mathrm{e}}$-fraction (the ratio of tachyonic and electric fine structure constants, cf. (2.18)) of the tachyon flux is actually absorbed, cf. Sect. 6 and [14, 15]. This requires a rescaling of the electron count n_1 (as calculated

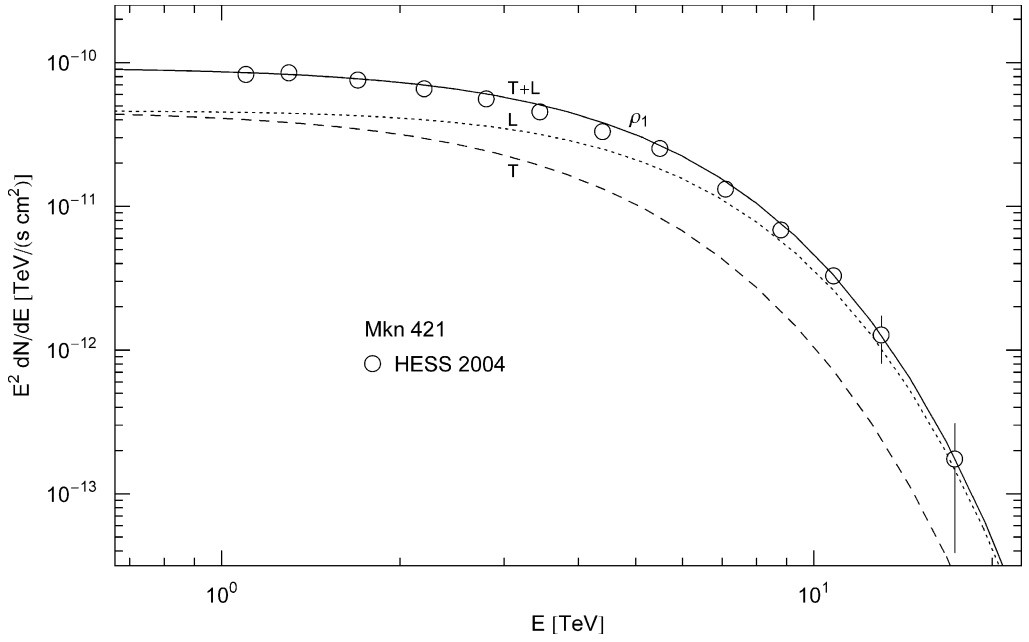

Fig. 6. Spectral map of Mkn 421 ($z \approx 0.031$). Data points from HESS [42], see also [43, 44]. The spectral fit T + L is a cascade ρ_1 generated by an electron distribution specified in Table 1. The transversal and longitudinal fluxes radiated are labeled T and L. Compared to the BL Lacs in Figs. 3–5, there is no apparent correlation between spectral curvature and redshift, which suggests that the curvature is generated by the electron population in the galactic nucleus rather than intergalactic absorption

from (5.2)), so that the actual number of radiating electrons is $n_1^{\rm e} := n_1\alpha_{\rm e}/\alpha_{\rm q} \approx 7.3\times 10^{10} n_1$.

In Table 1, we indicate the flux amplitude $\hat{n}_1$ obtained from the spectral fit, as well as the renormalized electron count $n_1^{\rm e}$ depending on the distance estimate. In the table, we drop the subscript 1 in $\hat{n}_1$, $n_1^{\rm e}$, and γ_1, and denote the density $\mathrm{d}\rho^{\rm B}_{\alpha,\beta}$ by ρ_1 (or $\rho_{i=1,2,3}$ in cascade spectra, cf. after (5.3)). This density ρ_1 is defined by parameters $(\alpha, \beta, \gamma_1, \hat{n}_1 \to n_1)$ extracted from the spectral fit. The distance estimates of the four low-z AGNs in Table 1 are based on $d \sim cz/H_0$, with $c/H_0 \approx 4.4\times 10^3\,$Mpc, that is, $h_0 \approx 0.68$, cf. [16]. The redshifts are quoted in the respective figure captions. The recessional speed, roughly cz, is already above the radiation threshold, cf. after (2.25), but this velocity component is negligible for the ultra-relativistic electron populations generating the γ-ray spectra. The source count in the surface field of the Crab pulsar is $n^{\rm e} \approx 2.6\times 10^{49}$, cf. [15], to be compared to 1.9×10^{50} obtained here for the whole remnant, cf. Table 1. A count of 1.3×10^{51} electrons/positrons in the nebula was derived from an electromagnetic synchrotron–inverse-Compton model in [17]. The source numbers listed in Table 1 are lower bounds based on γ-ray emission only. The tachyonic fine structure constant enters as a square in the number count, once via (5.2) when inferring the preliminary count n_1 from the spectral fit, and a second time when rescaling this count to obtain the actual source number $n_1^{\rm e}$. The tachyonic fine structure constant is an independent estimate from Lamb shifts in hydrogenic ions [1], and it is noteworthy that tachyonic and electromagnetic spectral fits result in comparable source counts. The cutoff in the electron energy is much higher compared to Compton fits, compensating the small tachyonic fine structure constant in the spectral density and absorption probability.

In the case of a thermal electron distribution ($\alpha = -2$ in (3.1) and (3.2)), we may identify $\beta = mc^2/(kT) \approx 5.93\times 10^9/T\,[\mathrm{K}]$, or $kT\,[\mathrm{keV}] \approx 511/\beta$. We use this definition of electron temperature also for other electron indices. kT is the cutoff energy at which the exponential decay sets in. At high temperature, the density (3.1) is peaked at $\gamma_{\rm peak} \approx -\alpha/\beta$, provided that $\alpha < 0$ and $\beta \ll |\alpha|$; the peak is followed by exponential decay. The bulk of the fermionic densities (3.2) is likewise located at about this $\gamma_{\rm peak}$. If $\alpha > 0$, the electron density is monotonically decreasing, at first as a power law and exponentially beyond kT. Positive electron indices occur in the shock-heated plasmas of the SNRs, cf. Table 1. Nearly straight power-law slopes, as seen in the TeV range of Figs. 1 and 2, can only emerge for electron indices $\alpha > 1$, cf. (4.10)–(4.12). The crossover energy from the GeV plateau into the power-law slope is determined by the lower edge γ_1 of electronic Lorentz factors in the blast wave. If $\alpha < 1$, the GeV plateau is followed by exponential decay, cf. the flare spectra in Figs. 3–6.

The cutoff kT in the electron energy is listed in Table 1, for each electron population generating a cascade in the γ-ray wideband, cf. after (5.3). These cutoffs are to be compared to the spectral breaks in the cosmic-ray spectrum, occurring at $10^{3.5}$ TeV, $10^{5.8}$ TeV, and 10^7 TeV, dubbed knee, second knee, and ankle, respectively [18, 19]. In all four BL Lacs as well as in the remnant RX J1713.7–3946, there are electron populations with energies reaching the knee of the cosmic-ray spectrum. In the Crab, the electron energies even extend to the second knee. As for protonic source particles, the cut-

Table 1. Electron distributions ρ_i generating the tachyonic cascade spectra of the supernova remnants and active galactic nuclei in Figs. 1–6. Each ρ_i stands for a Boltzmann power-law density $\mathrm{d}\rho^{\mathrm{B}}_{\alpha,\beta}(\gamma)$ defined by parameters $(\alpha,\beta,\gamma,\hat{n})$, cf. (3.1). α is the electronic power-law index, β the cutoff parameter in the Boltzmann factor, and γ the lower edge of Lorentz factors in the electronic source population ρ_i. $\hat{n}$ is the amplitude of the tachyon flux generated by ρ_i, from which the electron count n^{e} is inferred, cf. (5.2). d is the distance to the SNR or BL Lac; the estimate for the remnant RX J1713.7–3946 is taken from [20, 21]. kT is the electron temperature. The blazar spectra are thermal flare spectra with electron index $\alpha=-2$. The entry μ in the γ column denotes the electronic Lorentz factor defining the radiation threshold, cf. after (3.2). The cascade spectra labeled ρ_i in Figs. 1–6 are obtained by averaging the tachyonic radiation densities (2.22) with the electron distributions ρ_i, cf. Sects. 3 and 5; the parameters $(\alpha,\beta,\gamma,\hat{n})$ of each ρ_i are extracted from the spectral fit

	α	β	γ	$\hat{n}$	d (kpc)	n^{e}	kT (TeV)
SNRs							
Crab Nebula					2		
ρ_1	1.7	2.15×10^{-13}	2.3×10^{8}	6.0×10^{-3}		1.4×10^{48}	2.4×10^{6}
ρ_2	0.3	5.38×10^{-5}	1.0×10^{3}	0.2		4.6×10^{49}	9.5×10^{-3}
ρ_3	−1.1	8.6×10^{-3}	40	0.62		1.4×10^{50}	5.9×10^{-5}
RX J1713.7–3946					1		
ρ_1	1.2	3.52×10^{-12}	6.3×10^{8}	2.1×10^{-3}		1.2×10^{47}	1.5×10^{5}
ρ_2	0.8	9.35×10^{-5}	3.3×10^{4}	5.0×10^{-3}		2.9×10^{47}	5.5×10^{-3}
BL Lacs							
H1426+428					5.7×10^{5}		
ρ_1	−2	6.94×10^{-10}	μ	2.1×10^{-4}		3.9×10^{57}	740
ρ_2	−2	1.26×10^{-8}	μ	5.0×10^{-3}		9.3×10^{58}	41
1ES 1959+650					2.1×10^{5}		
ρ_1	−2	6.94×10^{-10}	μ	1.2×10^{-2}		3.1×10^{58}	740
ρ_2	−2	3.47×10^{-8}	μ	0.7		1.8×10^{60}	15
Mkn 501					1.5×10^{5}		
ρ_1	−2	6.62×10^{-10}	μ	1.0×10^{-2}		1.3×10^{58}	770
Mkn 421					1.4×10^{5}		
ρ_1	−2	1.21×10^{-9}	μ	1.0×10^{-2}		1.1×10^{58}	420

off energies in Table 1 have to be multiplied with 1.8×10^3, the proton/electron mass ratio, so that we arrive in the 10^{21}eV region, at ultra-high-energy protons in the two Galactic SNRs. (The tachyon/electron mass ratio in the spectral functions (3.7)–(3.10) has to be replaced by $m_{\mathrm{t}}/m_{\mathrm{p}}\approx 2.3\times10^{-6}$. In Figs. 1–6, however, this is not really necessary, since even the tachyon/electron ratio is too small to noticeably affect the high-energy spectral maps.)

Wideband cascade spectra are obtained by averaging over multiple electron populations,

$$\langle p^{\mathrm{T,L}}(\omega)\rangle^{\mathrm{B}} := \sum_i \langle p^{\mathrm{T,L}}(\omega;\gamma_i,n_i)\rangle^{\mathrm{B}}_{\alpha_i,\beta_i},$$
$$E^2\frac{\mathrm{d}N^{\mathrm{T,L}}(E)}{\mathrm{d}E} := \frac{\omega}{4\pi d^2}\langle p^{\mathrm{T,L}}(\omega)\rangle^{\mathrm{B}}. \qquad (5.3)$$

The normalization factors $A^{\mathrm{B}}_{\alpha_i,\beta_i}(\gamma_i,n_i)$ of the individual averages in the series (5.3) are calculated via

$$n_i = A^{\mathrm{B}}_{\alpha_i,\beta_i}(\gamma_i,n_i)\int_{\gamma_i}^{\infty}\mathrm{d}\rho^{\mathrm{B}}_{\alpha_i,\beta_i}(\gamma)\,, \qquad (5.4)$$

where n_i is the electron count and γ_i the smallest Lorentz factor in the population defined by density $\mathrm{d}\rho^{\mathrm{B}}_{\alpha_i,\beta_i}$. The electron numbers n_i (attached to a power-law index α_i, temperature $\beta_i=mc^2/(kT_i)$, and interval boundary γ_i, cf. (3.1)) determine the weights in the linear combination (5.3). Each density $\langle p^{\mathrm{T,L}}\rangle^{\mathrm{B}}_{\alpha_i,\beta_i}$ generates a cascade, labeled by $\rho_{i=1,2,3}$ in the figures. The spectral maps of the Markarian galaxies in Figs. 5 and 6 are not wideband; there is only one electron distribution and thus only one cascade ρ_1 for each flaring state. Fermi cascades are obtained in the same way, the multiple average $\langle p^{\mathrm{T,L}}(\omega)\rangle^{\mathrm{F}}$ in (5.3) being assembled with $\langle p^{\mathrm{T,L}}\rangle^{\mathrm{F}}_{\alpha_i,\beta_i}$ and $\mathrm{d}\rho^{\mathrm{F}}_{\alpha_i,\beta_i}$, cf. (3.2) and after (3.17).

If the polarization is not observed, we may add the transversal and longitudinal densities, writing $\langle p^{\mathrm{T+L}}\rangle^{\mathrm{B}} := \langle p^{\mathrm{T}}\rangle^{\mathrm{B}}+\langle p^{\mathrm{L}}\rangle^{\mathrm{B}}$ for the energy density and $N^{\mathrm{T+L}} := N^{\mathrm{T}}+N^{\mathrm{L}}$ for the number flux in (5.1) and (5.3). In the figures, we show the E^2-scaled unpolarized flux density, $E^2\mathrm{d}N^{\mathrm{T+L}}/\mathrm{d}E$ (solid line T + L), fitted to the data points. The individual averages in series (5.3) generate cascades drawn as dashed or dotted lines. (We always plot the E^2-scaled differential number flux, cf. (5.1), in this case the unpolarized flux from the individual source populations.) The cascades are labeled by ρ_i like the electron densities in Table 1 generating them. Each electron density ρ_i

is defined by parameters $(\alpha_i, \beta_i, \gamma_i, \hat{n}_i)$ obtained from the spectral fit and listed in the table, cf. after (5.2). The unpolarized tachyon flux, drawn as a solid line labeled T + L, is found by adding the cascade spectra ρ_i.

The rescaled transversal and longitudinal flux densities, $E^2 \mathrm{d}N^{\mathrm{T,L}}/\mathrm{d}E$, are depicted as dot-dashed (T) and double-dot-dashed (L) curves. The unpolarized flux T + L can also be obtained by adding these curves. The differential energy flux is $E\mathrm{d}N/\mathrm{d}E$. We have here dropped the possible superscripts T, L, or T + L, and do the same in the figures, labeling the respective curves with these letters instead. The E^2-scaled number flux, $E^2\mathrm{d}N/\mathrm{d}E$ (plotted in the figures), has no common conservation law associated with it, but this rescaling is frequently used in double-logarithmic plots of TeV spectra to render the curvature of steep spectral slopes better visible, and it is in this rescaling that spectral plateaus emerge in the GeV band.

6 Conclusion

We have derived the superluminal spectral densities generated by a Dirac current of freely moving charges, cf. Sect. 2, and explained the spectral averaging with Fermi and Boltzmann power laws, cf. Sect. 3. We have calculated the high- and low-temperature expansions of the averaged radiation densities, identified the asymptotic spectral parameters, and explained how they affect the power-law slopes, spectral plateaus, and spectral curvature in double-logarithmic plots, cf. Sect. 4. Finally, we have demonstrated that the high-energy spectral maps of SNRs and BL Lacs can be generated by tachyonic cascade spectra, cf. Sect. 5.

The purpose of this article is to provide evidence for the γ-ray spectra of supernova remnants and blazars to be tachyonic. Traditional radiation mechanisms such as inverse Compton scattering or pion decay fail to reproduce the extended GeV plateaus in the spectral maps [22, 31, 39]. The curvature present in the TeV flare spectra of BL Lacs is not correlated with distance, so that absorption due to interaction with background photons is not an attractive explanation for spectral curvature. Here, we have shown that the superluminal spectral densities of uniformly moving electrons are capable of producing the GeV plateaus in the spectral maps. The spectral curvature stems from the cutoff generated by the Boltzmann factor in the electron densities, which carries over to the averaged radiation densities, cf. (4.2). Intrinsic spectral curvature is also indicated by the strongly curved spectral maps of Galactic sources such as the pulsar wind nebula in SNR G0.9+0.1 and the TeV γ-ray sources HESS J1303–631 and HESS J1825–137, cf. [12].

We have studied superluminal radiation from electrons in straight uniform motion. Tachyonic synchrotron and cyclotron radiation were investigated in [6, 13, 14]. In the limit of large bending radius (zero-magnetic-field limit), the tachyonic synchrotron densities converge to the spectral densities (2.25) for uniform motion. A finite bending radius induces modulations in the spectral densities. At μG field strengths as encountered in the shock-heated plasmas of SNRs, these oscillations are quite small, just tiny ripples along the slope of densities (2.25) with increasing amplitude toward the spectral break, cf. [6]. If integrated over a thermal or power-law electron population, these oscillations are averaged out. In [13], we averaged synchrotron densities of SNRs with broken power laws, arriving at the classical limit of the spectral function (4.12). The conclusions of this paper, in particular the spectral maps in Figs. 1 and 2, do not change if the electron trajectories are bent by weak magnetic fields.

In this article, we have focused on γ-ray spectra. We conclude with some remarks on tachyonic X-rays. The negative mass-square in the dispersion relation results in a bound on the tachyonic wavelength. The tachyon mass, $m_{\mathrm{t}} \approx 2.15\,\mathrm{keV}/c^2$, gives a Compton wavelength of $\lambda^{\mathrm{C}} = 2\pi\hbar/(m_{\mathrm{t}}c) \approx 5.8\,\text{Å}$. Energy and wavelength are connected as $\lambda = 2\pi\hbar c/\sqrt{m_{\mathrm{t}}^2c^4 + \hbar^2\omega^2}$. The Compton wavelength is apparently the largest wavelength a tachyon can attain. At radio frequencies, the wavelength is constant and coincides with the Compton wavelength. Speed and energy of tachyonic quanta are related by $\hbar\omega = m_{\mathrm{t}}c^2(v^2/c^2 - 1)^{-1/2}$. At γ-ray energies, their speed is indistinguishably close to the speed of light. The basic difference to electromagnetic radiation is the longitudinally polarized flux component. The polarization of tachyons can be determined from the transversal and longitudinal ionization cross sections of Rydberg atoms, which peak at different scattering angles [45]. It is at hard-X-ray energies that a difference in the speed of photons and tachyons starts to emerge. If the tachyon flux is inferred from a grating spectrometer [46, 47], we have to use the above dispersion relation when parameterizing the observed differential count $\mathrm{d}N/\mathrm{d}\lambda$ with energy.

In Sect. 5, we pointed out that only a fraction $\alpha_{\mathrm{q}}/\alpha_{\mathrm{e}} \approx 1.4 \times 10^{-11}$ of the tachyon flux arriving at the detector is actually absorbed, so that the measured flux has to be rescaled with the ratio of electric and tachyonic fine structure constants. This rescaling applies to γ-ray spectra only, to frequencies much higher than the 2 keV tachyon mass, so that the mass-square can be dropped in the tachyonic dispersion relation. At X-ray energies, we have to rescale with the respective cross-section ratio, $\sigma_{\mathrm{e}}(\omega)/\sigma_{\mathrm{q}}(\omega)$, where σ_{e} is the electromagnetic cross section and σ_{q} its tachyonic counterpart. At hard-X-ray energies, the detection mechanism is usually ionization, generating scintillations in NaI(Tl) and CsI(Na) crystals of phoswich detectors [48, 49], or gas scintillations by ionization of xenon atoms in proportional counters [50, 51]. Tachyonic ionization cross sections of hydrogen-like ground states, that can be used for X-rays as well as γ-rays, have been calculated in [7]. At γ-ray energies, photonic and tachyonic dispersion relations coincide, and the cross-section ratio of the detection mechanism (such as ionization [52], Compton scattering [53], and pair production [54], the latter two quantified by Klein–Nishina and Bethe–Heitler cross sections) approaches a constant limit value $\alpha_{\mathrm{e}}/\alpha_{\mathrm{q}}$, which amounts to an overall rescaling of the tachyonic flux amplitude. By contrast, at X-ray energies, we have to rescale the tachyonic flux density with the energy-dependent cross-section ratio, which affects the shape of the spectral maps.

Acknowledgements. The author acknowledges the support of the Japan Society for the Promotion of Science. The hospitality and stimulating atmosphere of the Centre for Nonlinear Dynamics, Bharathidasan University, Trichy, and the Institute of Mathematical Sciences, Chennai, are likewise gratefully acknowledged.

References

1. R. Tomaschitz, Eur. Phys. J. B **17**, 523 (2000)
2. R. Tomaschitz, Physica A **320**, 329 (2003)
3. J.A. Wheeler, R.P. Feynman, Rev. Mod. Phys. **17**, 157 (1945)
4. R. Tomaschitz, Class. Quantum Grav. **18**, 4395 (2001)
5. R. Tomaschitz, Physica A **307**, 375 (2002)
6. R. Tomaschitz, Eur. Phys. J. C **45**, 493 (2006)
7. R. Tomaschitz, Eur. Phys. J. D **32**, 241 (2005)
8. N.M. Lloyd, V. Petrosian, Astrophys. J. **511**, 550 (1999)
9. N.M. Lloyd, V. Petrosian, R.S. Mallozzi, Astrophys. J. **534**, 227 (2000)
10. N.M. Lloyd-Ronning, V. Petrosian, Astrophys. J. **565**, 182 (2002)
11. V. Petrosian, Astrophys. J. **557**, 560 (2001)
12. R. Tomaschitz, Ann. Phys. (2007) DOI: 10.1016/j.aop.2006.11.005
13. R. Tomaschitz, Physica A **335**, 577 (2004)
14. R. Tomaschitz, Astropart. Phys. **23**, 117 (2005)
15. R. Tomaschitz, Astropart. Phys. (2007) DOI:10.1016/j.astropartphys.2006.09.003
16. R. Tomaschitz, Int. J. Theor. Phys. **44**, 195 (2005)
17. O.C. de Jager et al., Astrophys. J. **457**, 253 (1996)
18. M. Nagano, A.A. Watson, Rev. Mod. Phys. **72**, 689 (2000)
19. W.-M. Yao et al., J. Phys. G **33**, 1 (2006)
20. Y. Fukui et al., Publ. Astron. Soc. Jpn. **55**, L61 (2003)
21. Y. Moriguchi et al., Astrophys. J. **631**, 947 (2005)
22. J.C. Ling, W.A. Wheaton, Astrophys. J. **598**, 334 (2003)
23. L. Kuiper et al., Astron. Astrophys. **378**, 918 (2001)
24. R. Much et al., Astron. Astrophys. Suppl. Ser. **120**, 703 (1996)
25. R.D. van der Meulen et al., Astron. Astrophys. **330**, 321 (1998)
26. R.C. Hartman et al., Astrophys. J. Suppl. **123**, 79 (1999)
27. M. de Naurois et al., Astrophys. J. **566**, 343 (2002)
28. S. Oser et al., Astrophys. J. **547**, 949 (2001)
29. F. Aharonian et al., Astrophys. J. **614**, 897 (2004)
30. F. Aharonian et al., Astron. Astrophys. **457**, 899 (2006)
31. O. Reimer, M. Pohl, Astron. Astrophys. **390**, L43 (2002)
32. R. Enomoto et al., Nature **416**, 823 (2002)
33. F.A. Aharonian et al., Nature **432**, 75 (2004)
34. F.A. Aharonian et al., Astron. Astrophys. **449**, 223 (2006)
35. A. Djannati-Ataï et al., Astron. Astrophys. **391**, L25 (2002)
36. D. Petry et al., Astron. Astrophys. **580**, 104 (2002)
37. F. Aharonian et al., Astron. Astrophys. **403**, 523 (2003)
38. M.K. Daniel et al., Astrophys. J. **621**, 181 (2005)
39. H. Krawczynski et al., Astrophys. J. **601**, 151 (2004)
40. F.A. Aharonian et al., Astron. Astrophys. **349**, 11 (1999)
41. F.A. Aharonian et al., Astron. Astrophys. **366**, 62 (2001)
42. F. Aharonian et al., Astron. Astrophys. **437**, 95 (2005)
43. K. Okumura et al., Astrophys. J. **579**, L9 (2002)
44. M. Amenomori et al., Astrophys. J. **598**, 242 (2003)
45. R. Tomaschitz, J. Phys. A **38**, 2201 (2005)
46. J.W. den Herder et al., Astron. Astrophys. **365**, L7 (2001)
47. C.R. Canizares et al., Publ. Astron. Soc. Pac. **117**, 1144 (2005)
48. F. Frontera et al., Astron. Astrophys. Suppl. Ser. **122**, 357 (1997)
49. R.E. Rothschild et al., Astrophys. J. **496**, 538 (1998)
50. K. Makishima et al., Publ. Astron. Soc. Jpn. **48**, 171 (1996)
51. G. Manzo et al., Astron. Astrophys. Suppl. Ser. **122**, 341 (1997)
52. W.N. Johnson et al., Astrophys. J. Suppl. **86**, 693 (1993)
53. V. Schönfelder et al., Astrophys. J. Suppl. **86**, 657 (1993)
54. D.J. Thompson et al., Astrophys. J. Suppl. **86**, 629 (1993)